

## Spatially Variable Advection Correction of Doppler Radial Velocity Data

ALAN SHAPIRO,<sup>a,b</sup> JOSHUA G. GEBAUER,<sup>a</sup> NATHAN A. DAHL,<sup>c,d</sup> DAVID J. BODINE,<sup>e</sup>  
ANDREW MAHRE,<sup>a,e</sup> AND COREY K. POTVIN<sup>f,a</sup>

<sup>a</sup>*School of Meteorology, University of Oklahoma, Norman, Oklahoma*

<sup>b</sup>*Center for Analysis and Prediction of Storms, University of Oklahoma, Norman, Oklahoma*

<sup>c</sup>*Cooperative Institute for Mesoscale Meteorological Studies, University of Oklahoma, Norman, Oklahoma*

<sup>d</sup>*NOAA/NWS/Storm Prediction Center, University of Oklahoma, Norman, Oklahoma*

<sup>e</sup>*Advanced Radar Research Center, University of Oklahoma, Norman, Oklahoma*

<sup>f</sup>*NOAA/National Severe Storms Laboratory, University of Oklahoma, Norman, Oklahoma*

(Manuscript received 15 February 2020, in final form 7 August 2020)

**ABSTRACT:** Techniques to mitigate analysis errors arising from the nonsimultaneity of data collections typically use advection-correction procedures based on the hypothesis (frozen turbulence) that the analyzed field can be represented as a pattern of unchanging form in horizontal translation. It is more difficult to advection correct the radial velocity than the reflectivity because even if the vector velocity field satisfies this hypothesis, its radial component does not—but that component does satisfy a second-derivative condition. We treat the advection correction of the radial velocity ( $v_r$ ) as a variational problem in which errors in that second-derivative condition are minimized subject to smoothness constraints on spatially variable pattern-translation components ( $U$ ,  $V$ ). The Euler–Lagrange equations are derived, and an iterative trajectory-based solution is developed in which  $U$ ,  $V$ , and  $v_r$  are analyzed together. The analysis code is first verified using analytical data, and then tested using Atmospheric Imaging Radar (AIR) data from a band of heavy rainfall on 4 September 2018 near El Reno, Oklahoma, and a decaying tornado on 27 May 2015 near Canadian, Texas. In both cases, the analyzed  $v_r$  field has smaller root-mean-square errors and larger correlation coefficients than in analyses based on persistence, linear time interpolation, or advection correction using constant  $U$  and  $V$ . As some experimentation is needed to obtain appropriate parameter values, the procedure is more suitable for non-real-time applications than use in an operational setting. In particular, the degree of spatial variability in  $U$  and  $V$ , and the associated errors in the analyzed  $v_r$  field are strongly dependent on a smoothness parameter.

**KEYWORDS:** Data processing; Radars/Radar observations; Differential equations; Variational analysis

### 1. Introduction

The Taylor (1938) frozen-turbulence hypothesis is commonly used in physical science and engineering studies to infer the spatial distribution of flow variables from time series of those variables at fixed locations, study the statistical properties of turbulence, and mitigate analysis errors arising from the nonsimultaneity of data collections. According to this hypothesis, small-scale features in the velocity field can be idealized as patterns of unchanging form that are transported by a larger-scale “wind stream.” The validity of this hypothesis is a topic of continued interest (Uddin et al. 1997; Burghlea et al. 2005; Dennis and Nickels 2008; Li et al. 2009; Castro et al. 2011; Higgins et al. 2012; Wilczek et al. 2014; Creutin et al. 2015). Not surprisingly, the scales of motion bear on the validity of the hypothesis, and the validity degrades for longer time intervals.

Although Taylor (1938) described frozen turbulence as transport of small-scale features by a larger-scale wind, we consider here a broader meaning in which small-scale features are transported by larger-scale pattern-translation (advection) fields, without regard for how the translation is related to the air velocity. We refer to the transported variable as a passive scalar or a tracer. With attention restricted to horizontal advection, the frozen-turbulence hypothesis applied to a tracer

field  $R$  (representing, e.g., reflectivity) can be written in the functional form

$$R = R(x - Ut, y - Vt, z), \quad (1.1)$$

where  $x$ ,  $y$ , and  $z$  are Cartesian coordinates,  $t$  is time, and  $U$  and  $V$  are pattern-translation components. As noted, the latter may differ from the actual air velocity components ( $u$  and  $v$ ). If  $U$  and  $V$  are constant, then the equations that result from taking derivatives of (1.1) with respect to  $x$ ,  $y$ , and  $t$ , in turn, combine to give

$$\frac{\partial R}{\partial t} + U \frac{\partial R}{\partial x} + V \frac{\partial R}{\partial y} = 0. \quad (1.2)$$

Equation (1.2) can be written more succinctly as

$$\frac{DR}{Dt} = 0, \quad (1.3)$$

where  $D/Dt$  is the rate of change following the motion of the pattern; that is,  $D/Dt = \partial/\partial t + U\partial/\partial x + V\partial/\partial y$ . The paths of hypothetical (virtual) particles that move with the pattern-translation components  $U$  and  $V$  are the solutions  $x(t)$  and  $y(t)$  of  $Dx/Dt = U$  and  $Dy/Dt = V$ . For brevity we refer to such virtual-particle paths as trajectories, even though they do not generally represent the paths of actual air parcels.

The pattern-translation components  $U$  and  $V$  used in a variety of radar-, hydro-, and mesoscale-meteorological applications

Corresponding author: Alan Shapiro, ashapiro@ou.edu

DOI: 10.1175/JAS-D-20-0048.1

© 2020 American Meteorological Society. For information regarding reuse of this content and general copyright information, consult the AMS Copyright Policy ([www.ametsoc.org/PUBSReuseLicenses](http://www.ametsoc.org/PUBSReuseLicenses)).

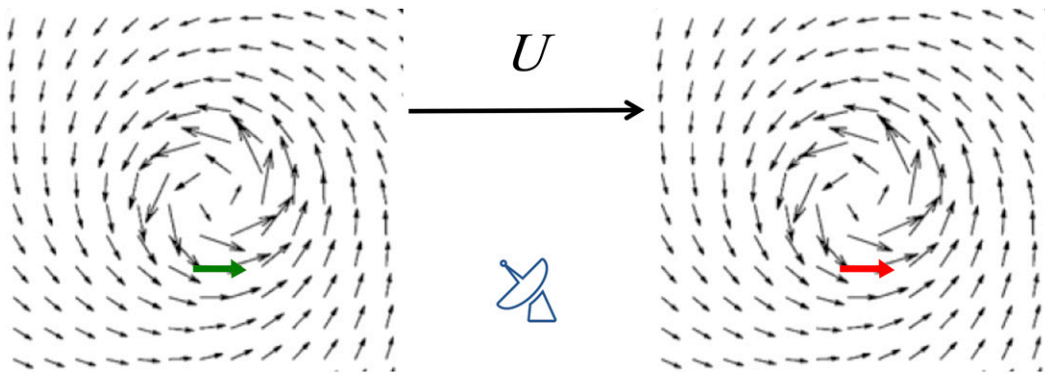


FIG. 1. A vortex of unchanging form translating past a radar provides a simple example of a radial velocity field that does not satisfy the frozen-turbulence hypothesis ( $Dv_r/Dt \neq 0$ ) even though the velocity field does satisfy that hypothesis ( $D\mathbf{u}/Dt = 0$ ). The same velocity vector that yields an inbound radial component (green,  $v_r < 0$ ) when the vortex is west of the radar yields an outbound radial component (red,  $v_r > 0$ ) when the vortex is east of the radar.

have been estimated visually (Heymsfield 1978; Carbone 1982; Hildebrand and Mueller 1985; Austin 1987; Dowell and Bluestein 1997; Wurman et al. 2007), obtained as wind profiles from a numerical weather prediction model (Mittermaier et al. 2004), calculated by cross-correlation analysis (Zawadzki 1973; Bellon and Zawadzki 1994; Fabry et al. 1994; Liu and Krajewski 1996; Anagnostou and Krajewski 1999; Gerstner and Heinemann 2008; Harrison et al. 2009; Nielsen et al. 2014; Thorndahl et al. 2014; Seo and Krajewski 2015), and derived from the minimization of a cost function in which (1.1), (1.2), or (1.3) is imposed as a weak constraint in a variational framework<sup>1</sup> (Gal-Chen 1982; Liu et al. 2004; Shapiro et al. 2010a, hereafter SWP10a). SWP10a repurposed a single-Doppler velocity retrieval (SDVR) algorithm similar to the frozen-turbulence-based SDVR algorithms of Tuttle and Foote (1990), Qiu and Xu (1992), Shapiro et al. (1995), Zhang and Gal-Chen (1996), Liou (1999, 2007), Lazarus et al. (2001), Liou and Luo (2001), and especially the variational echo tracking procedure of Laroche and Zawadzki (1995). In repurposing SDVR as advection correction, SDVR “winds” are interpreted as pattern-translation components rather than air velocity components. Moreover, while the tracer may be of limited interest in SDVR (beyond its use in obtaining the “winds”), it is of primary interest in advection correction—it is the variable being analyzed. SWP10a speculated that, in many cases, a frozen-turbulence-based SDVR procedure may work better as an advection-correction procedure than as a wind retrieval.

The advection correction of the Doppler radial velocity field  $v_r$  ( $\equiv \hat{\mathbf{r}} \cdot \mathbf{u}$ , where  $\mathbf{u}$  is the velocity field, and  $\hat{\mathbf{r}}$  is the unit vector in the direction of increasing radius  $r$ ) is more challenging than that of the reflectivity field because even if  $\mathbf{u}$  satisfies the frozen turbulence hypothesis ( $D\mathbf{u}/Dt = 0$ ), its radial component does not ( $Dv_r/Dt \neq 0$ ). A hypothetical flow that illustrates this property is shown in Fig. 1. Remarkably,

however, if  $D\mathbf{u}/Dt = 0$  with  $U$  and  $V$  constant,  $v_r$  satisfies (Gal-Chen 1982; Matejka 2002)

$$\frac{D^2(rv_r)}{Dt^2} = 0. \quad (1.4)$$

Unlike the expanded form of  $DR/Dt$  [which is (1.2)], the expanded form of (1.4) [see (2.2)] includes second derivatives with respect to space and time.

Attempts to mitigate analysis errors stemming from the nonsimultaneity of radar data collections often use advection-correction procedures in which  $U$  and  $V$  are treated as constant throughout the analysis domain or on each subdomain of a partitioned analysis domain. A notable exception is the SWP10a procedure, in which (1.3) is applied as a weak constraint along with smoothness constraints to obtain spatially varying  $U(x, y)$  and  $V(x, y)$  fields and an analyzed reflectivity field  $R(x, y, t)$  consistent with those fields and two time levels of input data. In a companion paper (Shapiro et al. 2010b, hereafter SWP10b), reflectivity data from a supercell storm were advection corrected to a time between the two data input times, and compared to data at that time. The spatially variable procedure produced analyses with smaller root-mean-square errors and larger correlation coefficients than analyses obtained with any pair of constant  $U$  and  $V$  parameters. Additional tests in SWP10b focused on advection correcting  $v_r$  using  $U$  and  $V$  obtained from (i) the spatially variable reflectivity-based procedure, or (ii) a range of imposed constant  $U$  and  $V$  values. Although the reflectivity-based procedure yielded generally good results, the errors in  $v_r$  were slightly larger than the errors obtained using the best of the constant  $U$  and  $V$  analyses. SWP10b suggested that better results might be obtained using a  $v_r$ -based procedure, that is, a procedure based on (1.4) instead of (1.3).

In this study we develop a frozen-turbulence-based advection-correction procedure for the radial velocity field in which the retrieved pattern translation components are spatially variable. An important application is to the analysis of non-simultaneously collected radial velocity data from two or more radars to common analysis times for use in multiple-Doppler wind syntheses of squall lines, supercells, tornadoes, and other

<sup>1</sup> We use the strong- and weak-constraint terminology of Sasaki (1970). A constraint that is imposed exactly is a strong constraint. A constraint that is imposed approximately (i.e., in a least squares error sense) is a weak constraint.

convective phenomena (Clark et al. 1980; Gal-Chen 1982; Chong et al. 1983; Hildebrand and Mueller 1985; Smull and Houze 1987; Bousquet et al. 2007; Wurman et al. 2010; Wienhoff et al. 2018; Oue et al. 2019; and many other studies).

The paper is arranged as follows. In section 2 we introduce the cost function whose minimization underpins the analysis. The Euler–Lagrange equations arising from the minimization of this cost function are derived in sections 3 and 4. The numerical procedures used to solve the Euler–Lagrange equations are described in section 5. In section 6, analytical data are used to verify that the computer code for the analysis procedure is error-free. Tests using data gathered by a mobile X-band Doppler radar, the Atmospheric Imaging Radar (AIR), of a band of heavy convective rainfall near El Reno, Oklahoma, on 4 September 2018, and a tornadic storm near Canadian, Texas, on 27 May 2015, are presented in section 7. Conclusions follow in section 8.

## 2. A cost function for advection correcting radial velocity data

As in SWP10a,b, we analyze data on a two-dimensional (2D) Cartesian grid on which gradually varying “large scale” advection fields  $U = U(x, y)$  and  $V = V(x, y)$  advect smaller-scale features in the data. The  $U$  and  $V$  fields are considered to be in a steady state. The analysis grid can be embedded on a surface of constant elevation angle [for data gathered in plan position indicator (PPI) mode] or on a surface of constant height [for data on constant-altitude PPI (CAPPI) surfaces]. The data on any analysis surface at any data input time are treated as if they were gathered instantaneously. A volume of data gathered as a sequence of surfaces can be analyzed sequentially, one surface at a time, with a single time stamp assigned for each surface. Some recently designed mobile Doppler radars can scan a single elevation angle in just a few seconds (e.g., French et al. 2014; Kurdzo et al. 2017; Wienhoff et al. 2018). However, operational radars such as those in the Weather Surveillance Radar-1988 Doppler (WSR-88D) network can take nearly 20 s to scan an elevation angle, even using a scan strategy designed for severe convective weather (Brown et al. 2005). In such cases, the peak displacement error on a PPI due to the assumed simultaneity of the data collection would be  $\sim 200$  m in a storm translating at a speed of  $\sim 10 \text{ m s}^{-1}$ . The significance of such an error may vary with the application, but should be minor if the scales of interest are  $\sim 1$  km or larger.

Our advection correction (analysis) procedure is based on (1.4). However, due to errors in the basic frozen turbulence constraint on which (1.4) is based ( $D\mathbf{u}/Dt = 0$ ), and additional errors in (1.4) stemming from the nonconstancy of  $U$  and  $V$ , we impose (1.4) as a weak constraint. Since  $r$  and  $v_r$  are paired in (1.4), it is convenient to work with the combined variable,

$$\Gamma \equiv rv_r. \quad (2.1)$$

For later use, we note that (1.4) expands out as

$$\begin{aligned} \frac{D^2\Gamma}{Dt^2} = & \Gamma_{tt} + 2U\Gamma_{xt} + 2V\Gamma_{yt} + 2UV\Gamma_{xy} + U^2\Gamma_{xx} + V^2\Gamma_{yy} \\ & + \left(\frac{\partial U}{\partial t} + U\frac{\partial U}{\partial x} + V\frac{\partial U}{\partial y}\right)\Gamma_x + \left(\frac{\partial V}{\partial t} + U\frac{\partial V}{\partial x} + V\frac{\partial V}{\partial y}\right)\Gamma_y, \end{aligned} \quad (2.2)$$

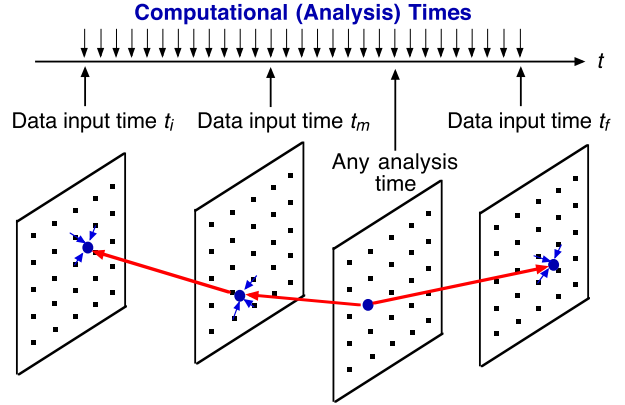


FIG. 2. Overview of the advection-correction procedure. During each outer iteration, the  $U$  and  $V$  fields are used to construct pattern-translation trajectories. A trajectory (example shown by red line) is launched forward and backward in time from every grid point at every analysis (computational) time. Radial velocity data are interpolated to each trajectory (blue arrows) at each of the three data input times. Between these times, the radial velocity is computed along each trajectory using (3.20a) and (3.20b). Since each trajectory originates from an analysis point at an analysis time, the radial velocities are now updated at every analysis point at every analysis time. The updated radial velocity (and updated  $D\Gamma/Dt$  and  $\Psi$ ) are used to update the coefficients in (5.1) and (5.2), which are then solved via SOR to update  $U$  and  $V$ .

where a subscript  $x$ ,  $y$ , or  $t$  on  $\Gamma$  denotes partial differentiation (e.g.,  $\Gamma_{xt} = \partial^2\Gamma/\partial x\partial t$ ). Although  $\partial U/\partial t$  and  $\partial V/\partial t$  are zero, it is convenient to retain those terms in (2.2).

The analysis domain is a rectangle with sides of length  $L_x$  parallel to the  $x$  axis, and  $L_y$  parallel to the  $y$  axis. The lower left corner of the domain is at the point  $(x_0, y_0)$ . The analysis window extends from an initial time  $t_i$  to an end time  $t_f$ . Radial velocity data are incorporated into the analysis at three data input times: the initial time  $t_i$ , the end time  $t_f$ , and an intermediate time  $t_m$  ( $t_i < t_m < t_f$ ). The radial velocities are analyzed to all of the analysis (computational) times within the analysis window (Fig. 2). For notational simplicity, we omit the limits of integration on all integrals that span the full analysis domain and analysis window, as in the (upcoming) cost function.

The analysis procedure determines  $U(x, y)$ ,  $V(x, y)$ , and  $\Gamma(x, y, t)$  fields that minimize a cost function

$$J = \iiint \left[ \alpha \left( \frac{D^2\Gamma}{Dt^2} \right)^2 + \kappa |\nabla U|^2 + \kappa |\nabla V|^2 \right] dx dy dt, \quad (2.3)$$

which accumulates the squared error in (1.4) and the squared gradients of  $U$  and  $V$  over the analysis domain and analysis window, while assimilating  $v_r$  observations at the

<sup>2</sup> At least three time levels of input data were also required in the  $v_r$ -based procedure of Gal-Chen (1982), in which a  $\partial^2 v_r / \partial t^2$  term was discretized. As shown in appendix A, minimizing (2.3) with  $v_r$  data incorporated at only two time levels yields meaningless results.

three data input times. As in [SWP10a,b](#),  $\alpha = \alpha(x, y, t)$  is a binary (0 or 1) data coverage function that satisfies the advection equation

$$\frac{D\alpha}{Dt} = 0. \quad (2.4)$$

The solution of (2.4) is  $\alpha(x, y, t) = \text{const}$  (along trajectories).<sup>3</sup> We assign  $\alpha = 0$  to trajectories that enter or leave the domain at any time during the analysis window or are in a data void at any data input time, and  $\alpha = 1$  to trajectories on which data are available at all three data input times. Due to the “filling in” effect of the Cressman filter used to interpolate raw radar data to the Cartesian analysis grid, the data coverage at a data input time may be more extensive on the analysis grid than on the radar grid. However, since  $\alpha(x, y, t)$  evolves as the numerical procedure iterates between evaluating  $\Gamma$  on trajectories, and

solving the elliptic equations for  $U$  and  $V$  (section 5), the form of  $\alpha(x, y, t)$  between data input times is not known until the procedure has converged. The  $\kappa|\nabla U|^2$  and  $\kappa|\nabla V|^2$  terms ( $\nabla$  is the horizontal gradient operator,  $\kappa$  is a weight function) confer spatial smoothness on  $U$  and  $V$ . However, unlike the smoothness weight ( $\beta$ ) in [SWP10a,b](#),  $\kappa$  is not constant, but increases with radius as  $\kappa = Kr^2$ , where  $K$  (which has units of  $\text{m}^2 \text{s}^{-4}$ ) is constant. The  $r^2$  factor in  $\kappa$  allows the smoothness terms to keep pace with the radial growth of terms in the weak-constraint form of frozen turbulence associated with the factor  $r$  in  $\Gamma \equiv rv_r$  [an  $r^2$  magnification factor for error in the weak-constraint form of frozen turbulence was noted by [Matejka \(2002\)](#)].

We minimize (2.3) using standard methods from the calculus of variations (e.g., [Elsgolc 1961](#); [Lanczos 1986](#)). Setting the first variation of  $J$  to zero, and using (2.2) yields

$$\begin{aligned} & \iiint \alpha \frac{D^2 \Gamma}{Dt^2} \frac{D^2 \delta \Gamma}{Dt^2} dx dy dt \\ & + \iiint \alpha \frac{D^2 \Gamma}{Dt^2} [2\delta U \Gamma_{xt} + 2\delta V \Gamma_{yt} + 2(U\delta V + V\delta U)\Gamma_{xy} + 2U\delta U \Gamma_{xx} + 2V\delta V \Gamma_{yy} \\ & + \left( \frac{\partial \delta U}{\partial t} + \delta U \frac{\partial U}{\partial x} + U \frac{\partial \delta U}{\partial x} + \delta V \frac{\partial U}{\partial y} + V \frac{\partial \delta U}{\partial y} \right) \Gamma_x \\ & + \left( \frac{\partial \delta V}{\partial t} + \delta U \frac{\partial V}{\partial x} + U \frac{\partial \delta V}{\partial x} + \delta V \frac{\partial V}{\partial y} + V \frac{\partial \delta V}{\partial y} \right) \Gamma_y] dx dy dt \\ & + \iiint \kappa \left( \frac{\partial U}{\partial x} \frac{\partial \delta U}{\partial x} + \frac{\partial U}{\partial y} \frac{\partial \delta U}{\partial y} + \frac{\partial V}{\partial x} \frac{\partial \delta V}{\partial x} + \frac{\partial V}{\partial y} \frac{\partial \delta V}{\partial y} \right) dx dy dt = 0. \end{aligned} \quad (2.5)$$

Since the variations  $\delta U$ ,  $\delta V$ , and  $\delta \Gamma$  are arbitrary and independent of each other, the integrals in (2.5) involving  $\delta U$ ,  $\delta V$ , and  $\delta \Gamma$  vanish independently of each other, and we obtain

$$\iiint \alpha \frac{D^2 \Gamma}{Dt^2} \frac{D^2 \delta \Gamma}{Dt^2} dx dy dt = 0, \quad (2.6)$$

$$\begin{aligned} & \iiint \alpha \frac{D^2 \Gamma}{Dt^2} \left( 2\Gamma_{xt} + 2V\Gamma_{xy} + 2U\Gamma_{xx} + \frac{\partial U}{\partial x} \Gamma_x + \frac{\partial V}{\partial x} \Gamma_y \right) \delta U dx dy dt \\ & + \iiint \alpha \frac{D^2 \Gamma}{Dt^2} \Gamma_x \left( \frac{\partial \delta U}{\partial t} + U \frac{\partial \delta U}{\partial x} + V \frac{\partial \delta U}{\partial y} \right) dx dy dt \\ & + \iiint \kappa \left( \frac{\partial U}{\partial x} \frac{\partial \delta U}{\partial x} + \frac{\partial U}{\partial y} \frac{\partial \delta U}{\partial y} \right) dx dy dt = 0, \end{aligned} \quad (2.7)$$

$$\begin{aligned} & \iiint \alpha \frac{D^2 \Gamma}{Dt^2} \left( 2\Gamma_{yt} + 2U\Gamma_{xy} + 2V\Gamma_{yy} + \frac{\partial U}{\partial y} \Gamma_x + \frac{\partial V}{\partial y} \Gamma_y \right) \delta V dx dy dt \\ & + \iiint \alpha \frac{D^2 \Gamma}{Dt^2} \Gamma_y \left( \frac{\partial \delta V}{\partial t} + U \frac{\partial \delta V}{\partial x} + V \frac{\partial \delta V}{\partial y} \right) dx dy dt \\ & + \iiint \kappa \left( \frac{\partial V}{\partial x} \frac{\partial \delta V}{\partial x} + \frac{\partial V}{\partial y} \frac{\partial \delta V}{\partial y} \right) dx dy dt = 0. \end{aligned} \quad (2.8)$$

<sup>3</sup> In the numerical solution procedure (section 5), trajectories are launched forward and backward in time from every analysis point at every analysis/computational time.

The Euler–Lagrange equations arising from (2.6)–(2.8) (sections 3 and 4) form a coupled set of differential equations for  $U$ ,  $V$ , and  $\Gamma$  that will be solved iteratively (section 5).

In [SWP10a](#), it was shown that many advection-correction procedures based on the frozen-turbulence constraint are subject to solution nonuniqueness associated with temporal aliasing [e.g., the reflectivity-based procedures in [SWP10a,b](#), [Gal-Chen \(1982\)](#), [Laroche and Zawadzki \(1995\)](#), and [Germann and Zawadzki \(2002\)](#)]. A proof similar to that in [SWP10a](#) (not shown), establishes that the  $v_r$ -based procedure in the present study is also subject to solution nonuniqueness. If one suspects that multiple cost function minima are likely (e.g., if there are wavy features in the data), the prospect of multiple solutions can be explored by using multiple first guesses for  $U$  and  $V$ , as in [Shapiro et al. \(2015\)](#). Use of a low-resolution “scaling guess,” as in [Laroche and Zawadzki \(1995\)](#) and [Germann and Zawadzki \(2002\)](#), may also be desirable.

### 3. Euler–Lagrange equation for $\Gamma$

To facilitate the derivation of the Euler–Lagrange equation arising from (2.6), we introduce

$$F \equiv \alpha \frac{D^2 \Gamma}{Dt^2}, \quad (3.1)$$

and make repeated use of the identities

$$a \frac{Db}{Dt} = \frac{D}{Dt}(ab) - b \frac{Da}{Dt}, \quad \text{and} \quad (3.2)$$

$$\frac{Dc}{Dt} = \frac{\partial c}{\partial t} + \frac{\partial}{\partial x}(Uc) + \frac{\partial}{\partial y}(Vc) - \left( \frac{\partial U}{\partial x} + \frac{\partial V}{\partial y} \right) c, \quad (3.3)$$

where  $a$ ,  $b$ , and  $c$  are generally functions of  $x$ ,  $y$ , and  $t$ . Using (3.2) with  $a \equiv F$  and  $b \equiv D\delta\Gamma/Dt$ , the integrand in (2.6) becomes

$$\alpha \frac{D^2\Gamma}{Dt^2} \frac{D^2\delta\Gamma}{Dt^2} = F \frac{D^2\delta\Gamma}{Dt^2} = \frac{D}{Dt} \left( F \frac{D\delta\Gamma}{Dt} \right) - \frac{D\delta\Gamma}{Dt} \frac{DF}{Dt}. \quad (3.4)$$

Similarly, applying (3.2) with  $a \equiv DF/Dt$  and  $b \equiv \delta\Gamma$  to the last term in (3.4) yields

$$\alpha \frac{D^2\Gamma}{Dt^2} \frac{D^2\delta\Gamma}{Dt^2} = \delta\Gamma \frac{D^2F}{Dt^2} + \frac{D}{Dt} \left( F \frac{D\delta\Gamma}{Dt} - \delta\Gamma \frac{DF}{Dt} \right). \quad (3.5)$$

Applying (3.3) with  $c = c_1 \equiv FD\delta\Gamma/Dt - \delta\Gamma DF/Dt$  to the last term in (3.5) yields

$$\begin{aligned} \alpha \frac{D^2\Gamma}{Dt^2} \frac{D^2\delta\Gamma}{Dt^2} &= \frac{\partial c_1}{\partial t} + \frac{\partial}{\partial x}(Uc_1) + \frac{\partial}{\partial y}(Vc_1) \\ &+ \delta\Gamma \left[ \frac{D^2F}{Dt^2} + \left( \frac{\partial U}{\partial x} + \frac{\partial V}{\partial y} \right) \frac{DF}{Dt} \right] - \left( \frac{\partial U}{\partial x} + \frac{\partial V}{\partial y} \right) F \frac{D\delta\Gamma}{Dt}. \end{aligned} \quad (3.6)$$

Applying (3.2) with  $a \equiv (\partial U/\partial x + \partial V/\partial y)F$  and  $b \equiv \delta\Gamma$  to the last term in (3.6) yields

$$\begin{aligned} \alpha \frac{D^2\Gamma}{Dt^2} \frac{D^2\delta\Gamma}{Dt^2} &= \frac{\partial c_1}{\partial t} + \frac{\partial}{\partial x}(Uc_1) + \frac{\partial}{\partial y}(Vc_1) \\ &+ \delta\Gamma \left[ \frac{D^2F}{Dt^2} + 2 \left( \frac{\partial U}{\partial x} + \frac{\partial V}{\partial y} \right) \frac{DF}{Dt} + F \frac{D}{Dt} \left( \frac{\partial U}{\partial x} + \frac{\partial V}{\partial y} \right) \right] \\ &- \frac{D}{Dt} \left[ \left( \frac{\partial U}{\partial x} + \frac{\partial V}{\partial y} \right) F \delta\Gamma \right]. \end{aligned} \quad (3.7)$$

Applying (3.3) to the last term in (3.7) with  $c = c_2 \equiv (\partial U/\partial x + \partial V/\partial y)F\delta\Gamma$  yields

$$\begin{aligned} \alpha \frac{D^2\Gamma}{Dt^2} \frac{D^2\delta\Gamma}{Dt^2} &= \frac{\partial}{\partial t}(c_1 - c_2) + \frac{\partial}{\partial x}[U(c_1 - c_2)] + \frac{\partial}{\partial y}[V(c_1 - c_2)] \\ &+ \delta\Gamma \left[ \frac{D^2F}{Dt^2} + 2 \left( \frac{\partial U}{\partial x} + \frac{\partial V}{\partial y} \right) \frac{DF}{Dt} + F \frac{D}{Dt} \left( \frac{\partial U}{\partial x} + \frac{\partial V}{\partial y} \right) + F \left( \frac{\partial U}{\partial x} + \frac{\partial V}{\partial y} \right)^2 \right] \\ &\quad \underbrace{= (D/Dt + \partial U/\partial x + \partial V/\partial y)(D/Dt + \partial U/\partial x + \partial V/\partial y)F} \end{aligned} \quad (3.8)$$

Using the definitions of  $F$ ,  $c_1$ , and  $c_2$  in (3.8), passing  $\alpha$  through the  $D/Dt$  operator [justified by (2.4)], factoring the underbraced term in (3.8) as indicated beneath the brace, and substituting the resulting form in (2.6) yields

$$\begin{aligned} &\iint \delta\Gamma \alpha \left( \frac{D}{Dt} + \frac{\partial U}{\partial x} + \frac{\partial V}{\partial y} \right) \left( \frac{D}{Dt} + \frac{\partial U}{\partial x} + \frac{\partial V}{\partial y} \right) \frac{D^2\Gamma}{Dt^2} dx dy dt \\ &+ \underbrace{\iint \left\{ \alpha \left[ \frac{D^2\Gamma}{Dt^2} \frac{D\delta\Gamma}{Dt} - \delta\Gamma \left( \frac{D}{Dt} + \frac{\partial U}{\partial x} + \frac{\partial V}{\partial y} \right) \frac{D^2\Gamma}{Dt^2} \right] \right\}_{t_i}^{t_f} dx dy}_{\text{area integral}} \\ &+ \underbrace{\iint \left\{ U \alpha \left[ \frac{D^2\Gamma}{Dt^2} \frac{D\delta\Gamma}{Dt} - \delta\Gamma \left( \frac{D}{Dt} + \frac{\partial U}{\partial x} + \frac{\partial V}{\partial y} \right) \frac{D^2\Gamma}{Dt^2} \right] \right\}_{x_0}^{x_0+L_x} dy dt}_{\text{east/west boundary integral}} \\ &+ \underbrace{\iint \left\{ V \alpha \left[ \frac{D^2\Gamma}{Dt^2} \frac{D\delta\Gamma}{Dt} - \delta\Gamma \left( \frac{D}{Dt} + \frac{\partial U}{\partial x} + \frac{\partial V}{\partial y} \right) \frac{D^2\Gamma}{Dt^2} \right] \right\}_{y_0}^{y_0+L_y} dx dt}_{\text{north/south boundary integral}} \end{aligned} \quad (3.9)$$

The area integral in (3.9) is evaluated at the initial and end times of the analysis window, and vanishes independently of the other integrals. Both terms in the integrand vanish in data voids ( $\alpha = 0$ ), and the second term also vanishes where data are available since  $\delta\Gamma = 0$  there. To ensure that the first term,  $(D^2\Gamma/Dt^2)(D\delta\Gamma/Dt)$ , vanishes where data are available (noting that  $D\delta\Gamma/Dt$  does not have to vanish where  $\delta\Gamma$  vanishes), we take

$$\left. \frac{D^2\Gamma}{Dt^2} \right|_{t=t_i} = 0, \quad (3.10a)$$

and

$$\left. \frac{D^2\Gamma}{Dt^2} \right|_{t=t_f} = 0, \quad (3.10b)$$

which is (1.4) imposed as a strong constraint at the initial and end times.

The integrand in the east/west boundary integral in (3.9) is proportional to  $\alpha$  and to the boundary-normal velocity component ( $U$ ). Clearly, the integrand is zero on any east/west boundary point on which  $U = 0$ . However, the integrand also vanishes on any east/west boundary point on which  $U \neq 0$ , since any trajectory launched at any analysis time from such a point is entering or leaving the domain (so  $\alpha = 0$ ). Thus, this boundary integral is identically zero. Similarly, it can be shown that the north/south boundary integral is identically zero.

The evaluation of the triple integral in (3.9) depends on the number  $n$  of data input times. The procedure corresponding to  $n = 3$  is described in detail in this section. In appendix A we show that an  $n = 2$  procedure yields meaningless results. A procedure based on arbitrary  $n (\geq 3)$  is outlined in appendix B, but its development is beyond the scope of this study.

For  $n = 3$ ,  $\Gamma$  is known (except in data voids) at each data input time, so  $\delta\Gamma = 0$  at times  $t_i$ ,  $t_m$ , and  $t_f$ . At analysis/computational times not coinciding with a data input time,  $\delta\Gamma$  is arbitrary and



the factor multiplying it in the triple integral in (3.9) must vanish. We thus obtain the Euler–Lagrange equation,

$$\alpha \left( \frac{D}{Dt} + \frac{\partial U}{\partial x} + \frac{\partial V}{\partial y} \right) \left( \frac{D}{Dt} + \frac{\partial U}{\partial x} + \frac{\partial V}{\partial y} \right) \frac{D^2 \Gamma}{Dt^2} = 0, \quad (3.11)$$

$(t \neq t_i, t_m, \text{ or } t_f),$

which we consider separately for analysis subwindows 1 ( $t_i < t < t_m$ ) and 2 ( $t_m < t < t_f$ ).

Equation (3.11) describes the evolution of  $\Gamma$  for virtual particles moving along pattern-translation trajectories. If data are missing on a trajectory at any data input time,  $\alpha = 0$  along that trajectory, and (3.11) is satisfied identically ( $0 = 0$ ) with no information obtained about  $\Gamma$ . If data are available on a trajectory at all data input times, then  $\alpha = 1$  along that trajectory, and we recast (3.11) as the system

$$\Theta \equiv \frac{D^2 \Gamma}{Dt^2}, \quad (3.12)$$

$$\Psi \equiv \frac{D\Theta}{Dt} + \left( \frac{\partial U}{\partial x} + \frac{\partial V}{\partial y} \right) \Theta, \quad (3.13)$$

$$\frac{D\Psi}{Dt} + \left( \frac{\partial U}{\partial x} + \frac{\partial V}{\partial y} \right) \Psi = 0. \quad (3.14)$$

For each trajectory, we solve (3.12)–(3.14) on subwindows 1 and 2, with subscripts 1 and 2 affixed to the solutions on the respective subwindows.

Equation (3.14) has the general solution

$$\Psi_1(t) = A_1 E_1(t), \quad (3.15a)$$

$$\Psi_2(t) = A_2 E_2(t), \quad (3.15b)$$

where  $A_1$  and  $A_2$  are constants of integration,

$$E_1(t) \equiv \exp \left[ - \int_{t_i}^t \text{div} \mathbf{U}(\tau') d\tau' \right], \quad (3.16a)$$

$$E_2(t) \equiv \exp \left[ - \int_{t_m}^t \text{div} \mathbf{U}(\tau') d\tau' \right], \quad (3.16b)$$

and  $\text{div} \mathbf{U}$  is the divergence of the pattern-translation velocity field  $\mathbf{U} \equiv (U, V)$ ,<sup>4</sup>

$$\text{div} \mathbf{U} \equiv \frac{\partial U}{\partial x} + \frac{\partial V}{\partial y}. \quad (3.17)$$

Although it should be clear from the context whether a time integral is evaluated at a fixed point or along a trajectory, we facilitate the distinction by using the symbol  $\tau$  (with primes) to represent the dummy integration variable in the time integrals that are evaluated along trajectories, as in (3.16a) and (3.16b).

With  $\Psi$  thus determined, (3.13) has the general solution

$$\Theta_1(t) = (A_1 t + B_1) E_1(t), \quad (3.18a)$$

$$\Theta_2(t) = (A_2 t + B_2) E_2(t), \quad (3.18b)$$

where  $B_1$  and  $B_2$  are constants of integration. Integrating the equations that result from applying (3.18a) and (3.18b) in (3.12) yields

$$\frac{D\Gamma_1}{Dt} = C_1 + A_1 \int_{t_i}^t \tau' E_1(\tau') d\tau' + B_1 \int_{t_i}^t E_1(\tau') d\tau', \quad (3.19a)$$

$$\frac{D\Gamma_2}{Dt} = C_2 + A_2 \int_{t_m}^t \tau' E_2(\tau') d\tau' + B_2 \int_{t_m}^t E_2(\tau') d\tau', \quad (3.19b)$$

where  $C_1$  and  $C_2$  are constants of integration. Integrating (3.19a) and (3.19b) yields the general solution

$$\Gamma_1(t) = C_1 t + D_1 + A_1 M_1(t) + B_1 N_1(t), \quad (3.20a)$$

$$\Gamma_2(t) = C_2 t + D_2 + A_2 M_2(t) + B_2 N_2(t), \quad (3.20b)$$

where  $D_1$  and  $D_2$  are constants of integration, and  $M_1$ ,  $M_2$ ,  $N_1$ , and  $N_2$  are defined by

$$M_1(t) \equiv \int_{t_i}^t \int_{t_i}^{\tau'} \tau'' E_1(\tau'') d\tau'' d\tau' = \int_{t_i}^t \tau' (t - \tau') E_1(\tau') d\tau', \quad (3.21a)$$

$$M_2(t) \equiv \int_{t_m}^t \int_{t_m}^{\tau'} \tau'' E_2(\tau'') d\tau'' d\tau' = \int_{t_m}^t \tau' (t - \tau') E_2(\tau') d\tau', \quad (3.21b)$$

$$N_1(t) \equiv \int_{t_i}^t \int_{t_i}^{\tau'} E_1(\tau'') d\tau'' d\tau' = \int_{t_i}^t (t - \tau') E_1(\tau') d\tau', \quad (3.22a)$$

$$N_2(t) \equiv \int_{t_m}^t \int_{t_m}^{\tau'} E_2(\tau'') d\tau'' d\tau' = \int_{t_m}^t (t - \tau') E_2(\tau') d\tau'. \quad (3.22b)$$

In arriving at (3.21a), (3.21b) and (3.22a), (3.22b), Cauchy's formula for repeated integration (Herrmann 2011) was used to express the double integrals as single integrals.

We now show how the conditions of the problem yield eight linear algebraic equations for eight unknowns—the eight integration constants in (3.20a) and (3.20b). Input data applied at the initial time in (3.20a) yield

$$C_1 t_i + D_1 = \Gamma(t_i). \quad (3.23)$$

Input data applied in (3.20a) and (3.20b) at the intermediate time<sup>5</sup> yield

$$C_1 t_m + D_1 + A_1 M_1(t_m) + B_1 N_1(t_m) = \Gamma(t_m) \quad (3.24)$$

and

$$C_2 t_m + D_2 = \Gamma(t_m). \quad (3.25)$$

Input data applied in (3.20b) at the end time yield

$$C_2 t_f + D_2 + A_2 M_2(t_f) + B_2 N_2(t_f) = \Gamma(t_f). \quad (3.26)$$

<sup>4</sup> Treated as field variables,  $U$ ,  $V$ , and  $\text{div} \mathbf{U}$  are in a steady state. However, due to their spatial variations, these same variables vary with time along trajectories. We obtain  $U$ ,  $V$ , and  $\text{div} \mathbf{U}$  along trajectories by interpolating their values from neighboring grid points to the location of the virtual particle tracing out the trajectory.

<sup>5</sup> To ensure continuity of  $\Gamma$  at time  $t_m$ , the input data are used twice: for  $\Gamma_1$  at the end of subwindow 1, and for  $\Gamma_2$  at the beginning of subwindow 2.

Applying (3.20a) in (3.10a) yields

$$A_1 t_i + B_1 = 0, \quad (3.27)$$

while applying (3.20b) in (3.10b) yields

$$A_2 t_f + B_2 = 0. \quad (3.28)$$

We have already accounted for continuity of  $\Gamma$  at time  $t_m$  (see footnote 5). Setting  $D\Gamma_1/Dt|_{t=t_m}$  from (3.19a) equal to  $D\Gamma_2/Dt|_{t=t_m}$  from (3.19b), yields a continuity condition for  $D\Gamma/Dt$  as

$$C_1 + A_1 \int_{t_i}^{t_m} \tau' E_1(\tau') d\tau' + B_1 \int_{t_i}^{t_m} E_1(\tau') d\tau' = C_2. \quad (3.29)$$

Setting  $\Theta_1(t_m)$  from (3.18a) equal to  $\Theta_2(t_m)$  from (3.18b), and noting from (3.16b) that  $E_2(t_m) = 1$ , we obtain a continuity condition for  $D^2\Gamma/Dt^2$  [which is  $\Theta$ , see (3.12)] as

$$(A_1 t_m + B_1) E_1(t_m) = A_2 t_m + B_2. \quad (3.30)$$

The eight equations [(3.23)–(3.30)] are solved by first re-writing (3.23), (3.25), (3.27), and (3.28) as

$$D_1 = \Gamma(t_i) - C_1 t_i, \quad (3.31)$$

$$D_2 = \Gamma(t_m) - C_2 t_m, \quad (3.32)$$

$$B_1 = -A_1 t_i, \quad (3.33)$$

$$B_2 = -A_2 t_f. \quad (3.34)$$

Applying (3.31) and (3.33) in (3.24) [with  $M_1(t_m)$  and  $N_1(t_m)$  obtained from (3.21a) and (3.22a), respectively] leads to

$$C_1 = -\frac{A_1}{t_m - t_i} \int_{t_i}^{t_m} (\tau' - t_i)(t_m - \tau') E_1(\tau') d\tau' + \frac{\Gamma(t_m) - \Gamma(t_i)}{t_m - t_i}. \quad (3.35)$$

Similarly, applying (3.32) and (3.34) in (3.26) [with  $M_2(t_f)$  and  $N_2(t_f)$  obtained from (3.21b) and (3.22b), respectively] leads to

$$C_2 = \frac{A_2}{t_f - t_m} \int_{t_m}^{t_f} (t_f - \tau')^2 E_2(\tau') d\tau' + \frac{\Gamma(t_f) - \Gamma(t_m)}{t_f - t_m}. \quad (3.36)$$

Applying (3.33) in (3.29) yields

$$C_2 = C_1 + A_1 \int_{t_i}^{t_m} (\tau' - t_i) E_1(\tau') d\tau'. \quad (3.37)$$

Applying (3.33) and (3.34) in (3.30) yields

$$A_2 = -A_1 \left( \frac{t_m - t_i}{t_f - t_m} \right) E_1(t_m). \quad (3.38)$$

Eliminating  $C_1$ ,  $C_2$ , and  $A_2$  in (3.35)–(3.38) yields  $A_1$  as

$$A_1 = \frac{(t_f - t_m) \left[ (t_m - t_i) \Gamma(t_f) - (t_f - t_i) \Gamma(t_m) + (t_f - t_m) \Gamma(t_i) \right]}{(t_f - t_m)^2 \int_{t_i}^{t_m} (\tau' - t_i)^2 E_1(\tau') d\tau' + (t_m - t_i)^2 E_1(t_m) \int_{t_m}^{t_f} (t_f - \tau')^2 E_2(\tau') d\tau'}. \quad (3.39)$$

One then gets  $C_1$  from (3.35),  $C_2$  from (3.37),  $A_2$  from (3.38),  $D_1$ ,  $D_2$ ,  $B_1$ , and  $B_2$  from (3.31)–(3.34), respectively, and  $\Gamma$  from (3.20a) and (3.20b).

#### 4. Euler–Lagrange equations for $U$ and $V$

When the second and third triple integrals in (2.7) (the integrals in which derivatives of  $\delta U$  appear) are integrated by parts, (2.7) becomes

$$\begin{aligned} & \iiint \left[ \alpha \Theta \left( 2\Gamma_{xt} + 2V\Gamma_{xy} + 2U\Gamma_{xx} + \frac{\partial U}{\partial x} \Gamma_x + \frac{\partial V}{\partial x} \Gamma_y \right) - \frac{\partial}{\partial t} (\alpha \Theta \Gamma_x) - \frac{\partial}{\partial x} (\alpha \Theta \Gamma_x U) - \frac{\partial}{\partial y} (\alpha \Theta \Gamma_x V) - \frac{\partial}{\partial x} \left( \kappa \frac{\partial U}{\partial x} \right) - \frac{\partial}{\partial y} \left( \kappa \frac{\partial U}{\partial y} \right) \right] \delta U dx dy dt \\ & + \underbrace{\iint [(\alpha \Theta \Gamma_x) \delta U]_{t_i}^{t_f} dx dy}_{\text{area integral}} + \underbrace{\iint \left[ \left( \alpha \Theta \Gamma_x U + \kappa \frac{\partial U}{\partial x} \right) \delta U \right]_{x_0}^{x_0+L_x} dy dt}_{\text{east/west boundary integral}} + \underbrace{\iint \left[ \left( \alpha \Theta \Gamma_x V + \kappa \frac{\partial U}{\partial y} \right) \delta U \right]_{y_0}^{y_0+L_y} dx dt}_{\text{north/south boundary integral}} = 0, \end{aligned} \quad (4.1)$$

where  $\Theta$  was defined in (3.12). Since  $\delta U$  is arbitrary ( $U$  is not known) and the right-hand side of (4.1) is zero, the integrals in (4.1) must vanish individually. The area integral (evaluated at the initial and end times,  $t_i$  and  $t_f$ ) vanishes in data voids ( $\alpha = 0$  there), and also where  $\alpha = 1$  since (3.10a) and (3.10b) (which are conditions on  $\Theta$ ) then apply. The first

term in both east–west and north–south boundary integrals vanishes since either  $\alpha$  or the boundary-normal velocity component is zero on the boundary (see discussion in section 3). To ensure that the second term in the boundary integrals vanishes, we impose the zero-normal gradient conditions:

$$\frac{\partial U}{\partial x} = 0 \quad \text{at} \quad x = x_0 \quad \text{and} \quad x = x_0 + L_x, \quad (4.2a)$$

$$\frac{\partial U}{\partial y} = 0 \quad \text{at} \quad y = y_0 \quad \text{and} \quad y = y_0 + L_y. \quad (4.2b)$$

Equation (4.1) now becomes

$$\begin{aligned} & \iiint \left[ \alpha \Theta \left( 2\Gamma_{xt} + 2V\Gamma_{xy} + 2U\Gamma_{xx} + \frac{\partial U}{\partial x}\Gamma_x + \frac{\partial V}{\partial x}\Gamma_y \right) \right. \\ & - \frac{\partial}{\partial x} \left( \kappa \frac{\partial U}{\partial x} \right) - \frac{\partial}{\partial y} \left( \kappa \frac{\partial U}{\partial y} \right) - \frac{\partial}{\partial t} (\alpha \Theta \Gamma_x) - \frac{\partial}{\partial x} (\alpha \Theta \Gamma_x U) \\ & \left. - \frac{\partial}{\partial y} (\alpha \Theta \Gamma_x V) \right] \delta U \, dx \, dy \, dt = 0. \end{aligned} \quad (4.3)$$

Using the product rule to expand the last three terms in (4.3) yields

$$\begin{aligned} & \iiint \left\{ \alpha \Theta \left( 2\Gamma_{xt} + 2V\Gamma_{xy} + 2U\Gamma_{xx} + \frac{\partial U}{\partial x}\Gamma_x + \frac{\partial V}{\partial x}\Gamma_y \right) - \frac{\partial}{\partial x} \left( \kappa \frac{\partial U}{\partial x} \right) \right. \\ & - \frac{\partial}{\partial y} \left( \kappa \frac{\partial U}{\partial y} \right) - \alpha \Theta \left[ \Gamma_{xt} + U\Gamma_{xx} + V\Gamma_{xy} + \Gamma_x \left( \frac{\partial U}{\partial x} + \frac{\partial V}{\partial y} \right) \right] \\ & \left. - \underbrace{\left( \frac{\partial \alpha}{\partial t} + U \frac{\partial \alpha}{\partial x} + V \frac{\partial \alpha}{\partial y} \right) \Theta \Gamma_x - \alpha \Gamma_x \left( \frac{\partial \Theta}{\partial t} + U \frac{\partial \Theta}{\partial x} + V \frac{\partial \Theta}{\partial y} \right)}_{=D\alpha/Dt=0} \right\} \delta U \, dx \, dy \, dt = 0. \end{aligned} \quad (4.4)$$

With many terms canceling, and its underbraced term vanishing because of (2.4), (4.4) becomes

$$\begin{aligned} & \iiint \left[ \alpha \Theta \left( \Gamma_{xt} + V\Gamma_{xy} + U\Gamma_{xx} + \frac{\partial V}{\partial x}\Gamma_y - \frac{\partial V}{\partial y}\Gamma_x \right) \right. \\ & \left. - \alpha \Gamma_x \frac{D\Theta}{Dt} - \frac{\partial}{\partial x} \left( \kappa \frac{\partial U}{\partial x} \right) - \frac{\partial}{\partial y} \left( \kappa \frac{\partial U}{\partial y} \right) \right] \delta U \, dx \, dy \, dt = 0. \end{aligned} \quad (4.5)$$

Equation (4.5) can be rewritten as

$$\begin{aligned} & \iiint \left[ \alpha \Theta \frac{\partial D\Gamma}{\partial t} - \alpha \Gamma_x \left( \frac{D}{Dt} + \frac{\partial U}{\partial x} + \frac{\partial V}{\partial y} \right) \Theta \right. \\ & \left. - \frac{\partial}{\partial x} \left( \kappa \frac{\partial U}{\partial x} \right) - \frac{\partial}{\partial y} \left( \kappa \frac{\partial U}{\partial y} \right) \right] \delta U \, dx \, dy \, dt = 0, \end{aligned} \quad (4.6)$$

or, in terms of the  $D\Gamma/Dt$ ,  $\Psi$ , and  $\Theta$  functions introduced in section 3,

$$\begin{aligned} & \iiint \left[ \alpha \left( \Theta \frac{\partial D\Gamma}{\partial t} - \Gamma_x \Psi \right) - \frac{\partial}{\partial x} \left( \kappa \frac{\partial U}{\partial x} \right) \right. \\ & \left. - \frac{\partial}{\partial y} \left( \kappa \frac{\partial U}{\partial y} \right) \right] \delta U \, dx \, dy \, dt = 0. \end{aligned} \quad (4.7)$$

Equation (4.7) yields the Euler–Lagrange equation for  $U$  as the elliptic equation<sup>6</sup>

$$\frac{\partial^2 U}{\partial x^2} + \frac{\partial^2 U}{\partial y^2} + \frac{1}{\kappa} \left( \frac{\partial \kappa}{\partial x} \frac{\partial U}{\partial x} + \frac{\partial \kappa}{\partial y} \frac{\partial U}{\partial y} \right) = \frac{1/\kappa}{t_f - t_i} \int_{t_i}^{t_f} \alpha \left( \Theta \frac{\partial D\Gamma}{\partial t} - \Gamma_x \Psi \right) dt. \quad (4.8)$$

Similarly, (2.8) generates the elliptic equation

$$\frac{\partial^2 V}{\partial x^2} + \frac{\partial^2 V}{\partial y^2} + \frac{1}{\kappa} \left( \frac{\partial \kappa}{\partial x} \frac{\partial V}{\partial x} + \frac{\partial \kappa}{\partial y} \frac{\partial V}{\partial y} \right) = \frac{1/\kappa}{t_f - t_i} \int_{t_i}^{t_f} \alpha \left( \Theta \frac{\partial D\Gamma}{\partial t} - \Gamma_y \Psi \right) dt, \quad (4.9)$$

subject to the boundary conditions

$$\frac{\partial V}{\partial x} = 0 \quad \text{at} \quad x = x_0 \quad \text{and} \quad x = x_0 + L_x, \quad (4.10a)$$

$$\frac{\partial V}{\partial y} = 0 \quad \text{at} \quad y = y_0 \quad \text{and} \quad y = y_0 + L_y. \quad (4.10b)$$

The integrals in (4.8) and (4.9) are evaluated at fixed locations, not along trajectories.

## 5. Numerical procedures

As in SWP10a,b, our solution technique is doubly iterative. The computer code iterates between updates of the analysis variable (in this case  $\Gamma$ ) and updates of  $U$  and  $V$ , and also solves for  $U$  and  $V$  iteratively, using successive over-relaxation (SOR). We refer to the iterations between updates of  $\Gamma$  and  $U$ ,  $V$  as outer iterations, and the SOR iterations as inner iterations. Within this framework, the treatment of the right-hand sides of (4.8) and (4.9) poses a dilemma. The simplest approach would be to replace  $\Gamma$ ,  $D\Gamma/Dt$ ,  $\Psi$ , and  $\Theta$  on the right-hand sides of (4.8) and (4.9) at the  $(N + 1)$ th outer iteration level by their solutions from the  $N$ th iteration level. However, as shown in appendix D, the resulting equations would, in general, have no solution. On the other hand, fully expanding  $D\Gamma/Dt$ ,  $\Psi$ , and  $\Theta$  into forms that explicitly display the  $U$ ,  $V$  fields [using (3.12) for  $\Theta$ , (3.13) for  $\Psi$ , and using  $D/Dt \equiv \partial/\partial t + U\partial/\partial x + V\partial/\partial y$ ], would produce over 100 terms, each of which would need to be integrated. A more tractable approach would be to expand the right-hand sides of (4.8) and (4.9) using (3.12) in the form  $\Theta = (\partial/\partial t + U\partial/\partial x + V\partial/\partial y)D\Gamma/Dt$ , but not expanding  $D\Gamma/Dt$  or  $\Psi$ , obtaining

<sup>6</sup> Second derivative terms in  $U$  and  $V$  which appear in the expansion of  $\Psi$  must be taken into account in the classification of (4.8) and (4.9) (appendix C).



$$\frac{\partial^2 U}{\partial x^2} + \frac{\partial^2 U}{\partial y^2} + \frac{1}{\kappa} \frac{\partial \kappa}{\partial x} \frac{\partial U}{\partial x} + \frac{1}{\kappa} \frac{\partial \kappa}{\partial y} \frac{\partial U}{\partial y} = a + bU + cV, \quad (5.1)$$

$$\frac{\partial^2 V}{\partial x^2} + \frac{\partial^2 V}{\partial y^2} + \frac{1}{\kappa} \frac{\partial \kappa}{\partial x} \frac{\partial V}{\partial x} + \frac{1}{\kappa} \frac{\partial \kappa}{\partial y} \frac{\partial V}{\partial y} = e + cU + gV, \quad (5.2)$$

where

$$a \equiv \frac{1/\kappa}{t_f - t_i} \int_{t_i}^{t_f} \alpha \left[ \left( \frac{\partial}{\partial x} \frac{D\Gamma}{Dt} \right) \left( \frac{\partial}{\partial t} \frac{D\Gamma}{Dt} \right) - \Gamma_x \Psi \right] dt, \quad (5.3a)$$

$$b \equiv \frac{1/\kappa}{t_f - t_i} \int_{t_i}^{t_f} \alpha \left( \frac{\partial}{\partial x} \frac{D\Gamma}{Dt} \right)^2 dt, \quad (5.3b)$$

$$c \equiv \frac{1/\kappa}{t_f - t_i} \int_{t_i}^{t_f} \alpha \left( \frac{\partial}{\partial x} \frac{D\Gamma}{Dt} \right) \left( \frac{\partial}{\partial y} \frac{D\Gamma}{Dt} \right) dt, \quad (5.3c)$$

$$e \equiv \frac{1/\kappa}{t_f - t_i} \int_{t_i}^{t_f} \alpha \left[ \left( \frac{\partial}{\partial y} \frac{D\Gamma}{Dt} \right) \left( \frac{\partial}{\partial t} \frac{D\Gamma}{Dt} \right) - \Gamma_y \Psi \right] dt, \quad (5.3d)$$

$$g \equiv \frac{1/\kappa}{t_f - t_i} \int_{t_i}^{t_f} \alpha \left( \frac{\partial}{\partial y} \frac{D\Gamma}{Dt} \right)^2 dt. \quad (5.3e)$$

As shown in [appendix D](#), the solution of (5.1) and (5.2) subject to the Neumann conditions (4.2a), (4.2b) and (4.10a), (4.10b) for any outer iteration level (with  $\Gamma$ ,  $D\Gamma/Dt$ , and  $\Psi$  known from the previous iteration) is unique. This simplifies the implementation of the SOR solver. However, this uniqueness result only pertains to the solution of (5.1) and (5.2) at any one outer iteration level. As discussed in [section 2](#), uniqueness of the overall converged solution for  $U$ ,  $V$ , and  $\Gamma$  cannot be ensured.

The analysis procedure is schematized in [Fig. 2](#). During the  $(N + 1)$ th outer iteration, a fourth-order Runge–Kutta method ([Press et al. 1992](#)) is used to construct the pattern-translation trajectories  $x(t)$ ,  $y(t)$  from the  $U$ ,  $V$  fields at the  $N$ th iteration.<sup>7</sup> Trajectories are launched forward and backward in time from every analysis point at every analysis time. At each data input time,  $v_r$  data (really  $\Gamma$ ) and  $\text{div}\mathbf{U}$  are bilinearly interpolated to each trajectory. If data are missing on a trajectory at any data input time, we set  $\alpha = 0$  for that trajectory. On trajectories for which data are available at all data input times ( $\alpha = 1$ ), we calculate  $\Gamma$  from (3.20a) and (3.20b),  $D\Gamma/Dt$  from (3.19a) and (3.19b), and  $\Psi$  from (3.15a) and (3.15b). Since a trajectory passes through each analysis point at each analysis time, this calculation also updates  $\Gamma$ ,  $D\Gamma/Dt$ , and  $\Psi$  at all analysis points at all analysis times. The updated variables are used to update the coefficients in (5.1) and (5.2). These equations are solved for  $U$  and  $V$  subject to boundary conditions (4.2a), (4.2b) and (4.10a), (4.10b) using SOR with an overrelaxation coefficient set to 1.95. If the maximum change in  $U$  or  $V$  from the  $N$ th to  $(N + 1)$ th outer iteration levels is less than a prescribed tolerance ( $\text{ToLOUT} = 0.001 \text{ m s}^{-1}$ ), the procedure is deemed to have converged; otherwise, the procedure returns to the trajectory

calculation step. If the procedure fails to converge, the nonconvergence can be manifested as  $U$ ,  $V$  values that oscillate (cycle) around unchanged values, or as continued growth of  $U$ ,  $V$  to unrealistically large values, with concomitant development of large data voids as virtual particles quickly leave the domain. In the former case, if the oscillation is of sufficiently small amplitude, the procedure can still provide good estimates of the radial velocity field.

Preliminary tests (not shown) with the AIR and the analytical datasets showed that a few ad hoc amendments could improve the basic procedure. For small enough values of  $K$ ,<sup>8</sup> a numerical instability prevented convergence of the overall procedure. Fortunately, for some of those cases, the instability could be prevented by setting  $U$ ,  $V$ , and  $\text{div}\mathbf{U}$  at the end of the  $(N + 1)$ th outer iteration level equal to a blend of  $U$ ,  $V$ , and  $\text{div}\mathbf{U}$  from the previous iteration and the corresponding solutions from the current iteration; that is,

$$f^{N+1} = (1 - \text{wgt})f^N + \text{wgt}\tilde{f}^{N+1}, \quad (5.4)$$

where  $\tilde{f}$  is an unblended field, and  $\text{wgt}$  is an underrelaxation parameter (we set  $\text{wgt} = 0.025$ ). This device allowed us to extend the lower range of  $K$  in our tests, but came at the cost of much slower SOR convergence for large  $K$ . Indeed, in preliminary uniform translation tests, the convergence rates in runs with relatively large  $K$  were so slow that the solver stopped iterating prematurely; the solution had “converged” even though the  $U$  and  $V$  fields fell well short of their true values. To mitigate this problem, we set the convergence tolerance ( $\text{ToLSOR}$ ) to a value much smaller than one might expect to be necessary,  $\text{ToLSOR} = 5 \times 10^{-8} \text{ m s}^{-1}$ , and allowed the SOR module up to  $10^7$  iterations to converge (though in most tests, convergence was achieved with far fewer iterations). Unless stated otherwise, these modifications/configurations were applied in all of the tests in [sections 6](#) and [7](#). Additionally, in the real data tests ([section 7](#)),  $D\Gamma/Dt$  was smoothed using a nine-point filter prior to its use in (5.3a)–(5.3e). In most of these tests, this filter had little impact on the accuracy of the analyzed  $v_r$  field, with differences in root-mean-square error (RMSE) between filtered and nonfiltered runs on the order of  $0.01 \text{ m s}^{-1}$ . However, the filter did slightly reduce the number of outer iterations required for convergence (typically by about 10%–20%) and, in a few cases, promoted convergence of an otherwise nonconverging analysis.

Although we have not developed a procedure to estimate appropriate values for  $K$ , an amplitude principle for  $K$  can be inferred from (2.3): if, for a dataset with radial velocity field  $v_r(x, y, t)$ , a smoothness constant  $K_1$  has been identified for

<sup>7</sup> Unless stated otherwise, the first guesses for  $U$  and  $V$  in our experiments (i.e., at the first iteration) are  $0 \text{ m s}^{-1}$ .

<sup>8</sup> We refer to “large” or “small” values of  $K$  in a relative sense, that is, with respect to a given dataset. A value of  $K$  large enough to produce nearly constant  $U$  and  $V$  in one dataset may be too small to produce nearly constant  $U$  and  $V$  in another dataset, even if the two datasets have the same spatial and temporal resolution (as in the two AIR datasets considered in [section 7](#)).

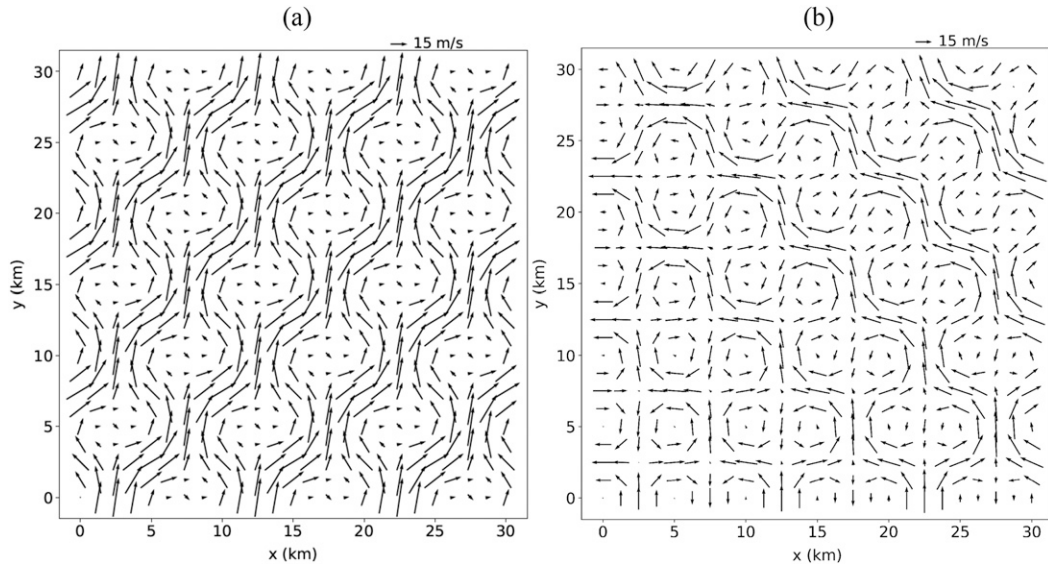


FIG. 3. Velocity vectors in the analytical data tests at the initial time ( $t = 0$  s). (a) An array of vortices is in uniform translation with  $U = 5 \text{ m s}^{-1}$  and  $V = 15 \text{ m s}^{-1}$ . (b) The array of vortices is itself rotating as a solid-body vortex. This solid-body vortex has angular velocity  $\Omega = 3 \times 10^{-4} \text{ s}^{-1}$ , and is centered on a virtual radar at the lower-left corner of the domain ( $x = 0 \text{ km}$ ,  $y = 0 \text{ km}$ ). The velocity field is constructed from (6.3) and (6.4) for (a), and (6.7)–(6.9) for (b).

which the retrieved  $U$  and  $V$  fields are deemed physically reasonable, then for a dataset with radial velocity field  $v_{r2}(x, y, t)$  having the same pattern as  $v_{r1}$  throughout the analysis window but an amplitude  $\varepsilon$  times that of  $v_{r1}$  ( $v_{r2} = \varepsilon v_{r1}$ ), the same  $U$  and  $V$  can be obtained using the smoothness constant  $K_2 = \varepsilon^2 K_1$ . Although the all-other-things-being-equal conditions for the validity of this principle can never be met in practice, the idea that larger values of  $K$  should be applied to datasets with larger radial velocity amplitudes may be useful.

## 6. Analytical data tests

The computer code for the procedure is verified using analytical data from an inviscid version of Taylor's array of counterrotating vortices (Rosenhead 1963, p. 139). The velocity field is 2D, and the vertical velocity component is zero. In the steady state, the Cartesian velocity components are given by

$$u(x, y) = AF(x)G(y), \quad v(x, y) = AH(x)I(y), \quad (6.1)$$

where  $A$  is the amplitude, the functions  $F(x)$ ,  $G(y)$ ,  $H(x)$ , and  $I(y)$  are defined by

$$\begin{aligned} F(x) &\equiv -\cos(kx), & G(y) &\equiv \sin(l y), & H(x) &\equiv \sin(kx), \\ I(y) &\equiv \cos(l y), \end{aligned} \quad (6.2)$$

where  $k$  and  $l$  are wavenumbers that control the size of the vortices in the array.

We conduct two types of tests. First, we suppose that the array translates with constant  $U$  and  $V$ . The velocity components then satisfy

$$\begin{aligned} u(x, y, t) &= U + AF[x^*(t)]G[y^*(t)], \\ v(x, y, t) &= V + AH[x^*(t)]I[y^*(t)], \end{aligned} \quad (6.3)$$

where  $x^*$  and  $y^*$  are the shifted coordinates,

$$x^*(t) \equiv x - Ut, \quad y^*(t) \equiv y - Vt. \quad (6.4)$$

A virtual radar at the origin of the coordinate system (at the ground,  $z = 0$ ) scanning the  $0^\circ$  elevation angle (the surface  $z = 0$ ) samples the radial velocity field as

$$v_r = \frac{x}{r}u(x, y, t) + \frac{y}{r}v(x, y, t), \quad (6.5)$$

where  $u$  and  $v$  are given by (6.3) and (6.4). Since  $U$  and  $V$  are constant, and the velocity components in (6.3) satisfy the frozen-turbulence constraint  $D\mathbf{u}/Dt = 0$  exactly, the corresponding radial-velocity component  $v_r$  should satisfy (1.4) exactly. Moreover, since  $U$  and  $V$  are constant,  $\nabla U = \nabla V = 0$  everywhere. Thus, if the code is error free, it should yield the correct  $U$ ,  $V$ , and  $\Gamma$  fields, apart from numerical discretization and integration errors: the analyzed fields yield a value of zero for the cost function (2.3) (which is clearly a minimum), and satisfy boundary conditions (4.2a), (4.2b) and (4.10a), (4.10b). Moreover, the same (correct) results should be obtained for any value of  $K$ .

In a second test, we consider the rotation of the vortex array by a solid body vortex centered on the radar. In this case, the radial component of the pattern translation  $V_r \equiv (xU + yV)/r$ , i.e., the right-hand side of (6.5) with  $u$  replaced by  $U$ , and  $v$  replaced by  $V$  is zero, the azimuthal component  $V_\theta \equiv (xV - yU)/r$  varies linearly with radius [ $V_\theta = \Omega r$ , where  $\Omega$  is the (constant) angular velocity],  $U$  and  $V$  vary spatially as

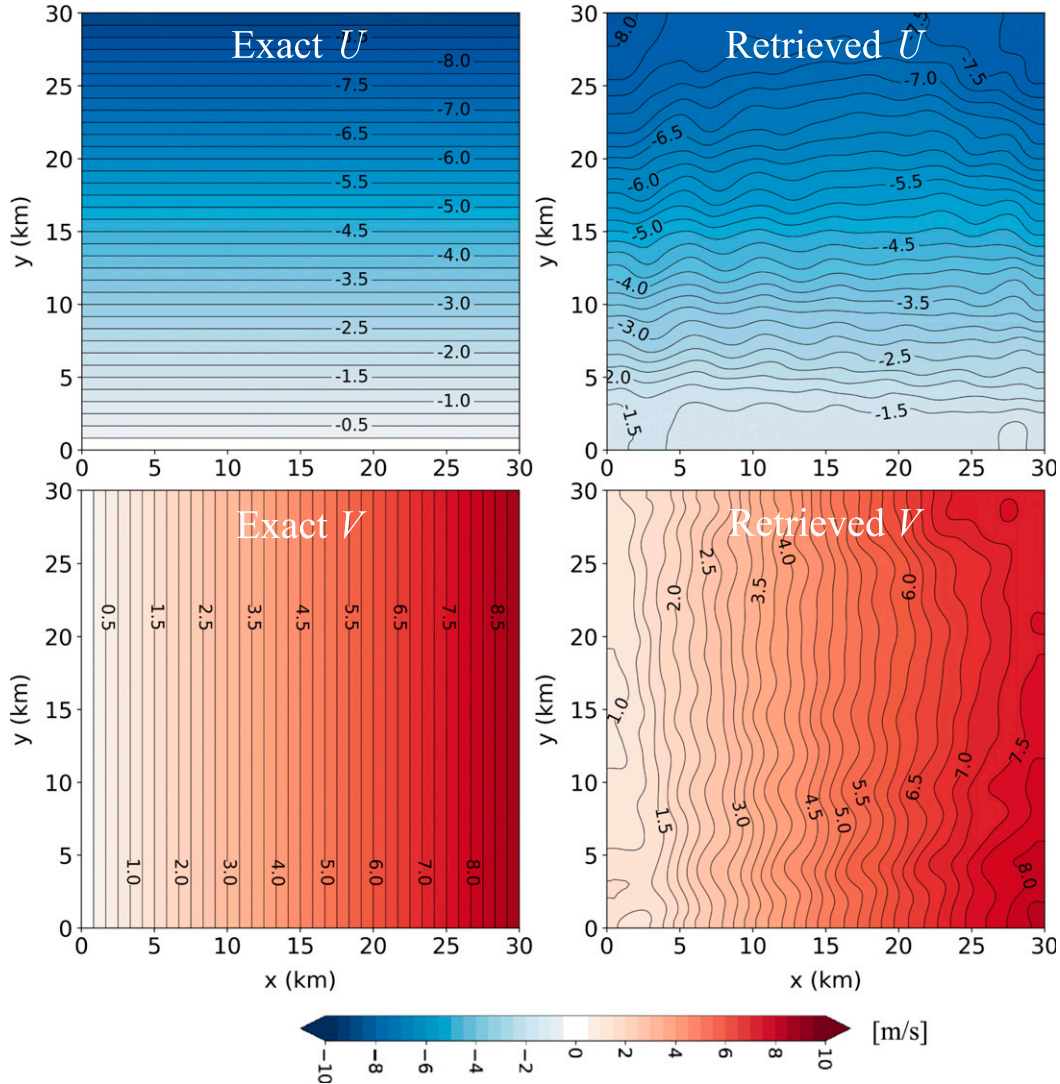


FIG. 4. (left) Exact analytical and (right) retrieved (top)  $U$  and (bottom)  $V$  pattern-translation fields from a test in which an array of vortices rotates as a solid body (see Fig. 3b). The smoothing parameter is  $K = 0.0002 \text{ m}^2 \text{ s}^{-4}$ .

$$U = -\Omega y, \quad V = \Omega x, \quad (6.6)$$

and the Cartesian velocity components satisfy

$$\begin{aligned} u(x, y, t) &= -\Omega y + AF[x^*(t)]G[y^*(t)], \\ v(x, y, t) &= \Omega x + AH[x^*(t)]I[y^*(t)], \end{aligned} \quad (6.7)$$

where

$$\begin{aligned} x^*(t) &= r \cos(\theta - \Omega t) = r \cos\theta \cos\Omega t + r \sin\theta \sin\Omega t \\ &= x \cos\Omega t + y \sin\Omega t, \end{aligned} \quad (6.8)$$

$$\begin{aligned} y^*(t) &= r \sin(\theta - \Omega t) = r \sin\theta \cos\Omega t - r \cos\theta \sin\Omega t \\ &= y \cos\Omega t - x \sin\Omega t. \end{aligned} \quad (6.9)$$

The radial velocities are obtained from (6.5), with  $u$  and  $v$  given by (6.7)–(6.9).

It can be shown that  $u$  and  $v$  in the uniform translation test [i.e., given by (6.3) and (6.4) with constant  $U$  and  $V$ ] satisfy the inviscid equations of motion exactly, but the  $u$  and  $v$  fields in the solid body vortex test [i.e., given by (6.7)–(6.9) with  $U$  and  $V$  satisfying (6.6)] do not. However, since the analyses are not constrained by the dynamical underpinnings of the flow (other than the assumption that the frozen-turbulence hypothesis is at least qualitatively valid), the failure of (6.7)–(6.9) to satisfy the equations of motion should not preclude their use in our tests. Of more concern, however, is that  $U, V$  fields satisfying (6.6) cannot satisfy all of the zero-normal gradient conditions (4.2a), (4.2b) and (4.10a), (4.10b). Thus, it will not be possible to retrieve  $U$  and  $V$  exactly in the solid body vortex test case. However, as we will see, we can retrieve  $U$  and  $V$  fields in good agreement with (6.6) away from computational boundaries.

In both sets of tests, we take  $A = 20 \text{ m s}^{-1}$ ,  $k = l = 2\pi/\lambda$ , and  $\lambda = 10 \text{ km}$ . The analysis domain is a square with sides of length

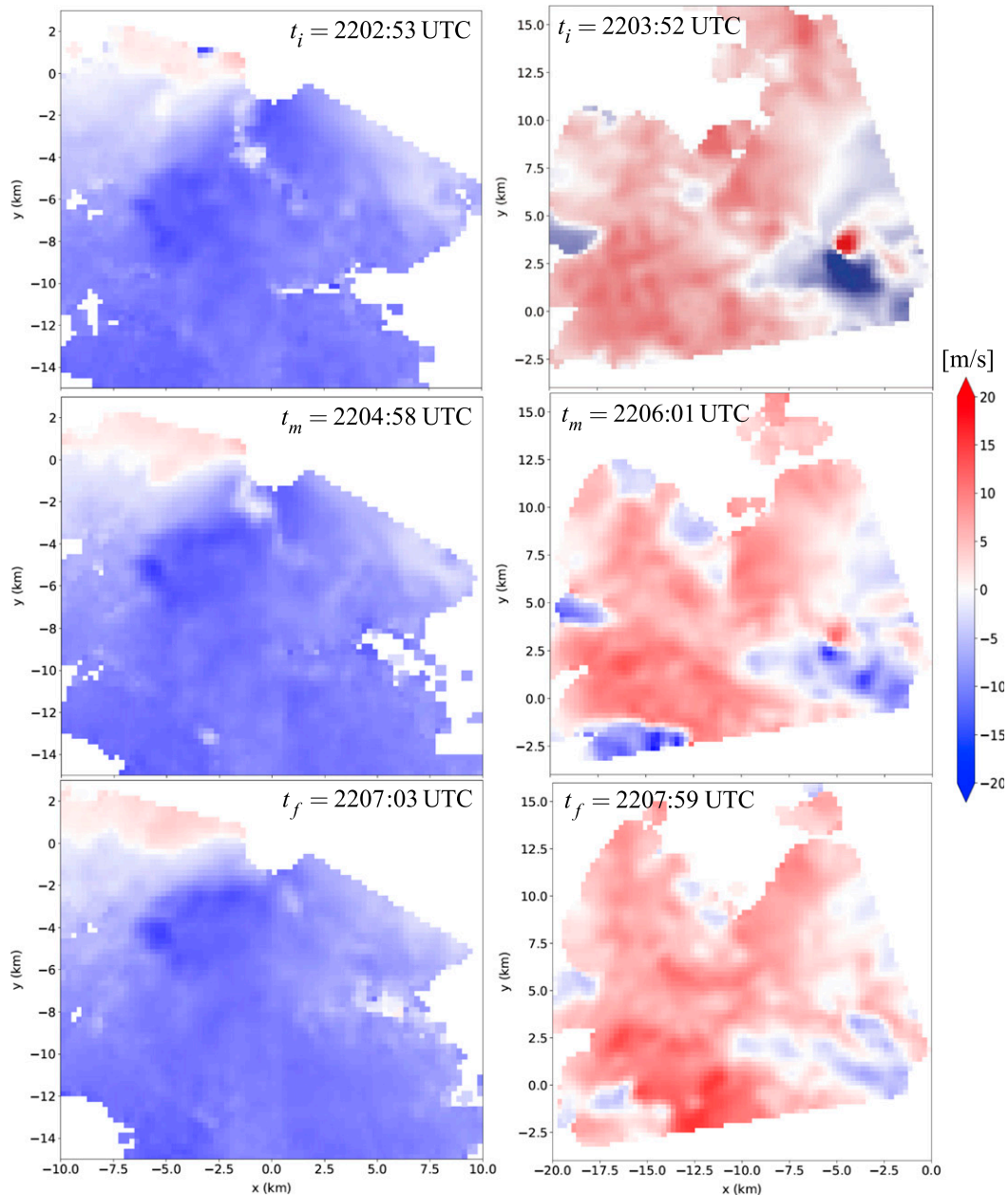


FIG. 5. The AIR  $v_r$  in (left) a convective rainband on 4 Sep 2018 and (right) a decaying tornado and its parent storm on 27 May 2015 at the three data input times: (top) initial time  $t_i$ , (middle) intermediate time  $t_m$ , and (bottom) end time  $t_f$ . The AIR is at  $x = 0$  km,  $y = 0$  km.

30 km, and a gridpoint spacing of  $\Delta x = \Delta y = 250$  m ( $121 \times 121$  points). The computational time step is  $\Delta t = 4$  s. The analysis window is 6 min, with data supplied at 3 min intervals. In the uniform translation tests, data are generated from (6.3) and (6.4) with  $U = 5$  m s $^{-1}$  and  $V = 15$  m s $^{-1}$ . In the solid body vortex tests, data are generated using (6.7)–(6.9) with  $\Omega = 3 \times 10^{-4}$  s $^{-1}$ . The velocity fields for these cases are shown in Fig. 3.

The  $U$ ,  $V$  fields retrieved in the uniform translation tests were nearly constant and nearly equal to their true values for a range of values of the smoothness parameter. In tests run with

$K = 0.5, 1, 5, 10, 50, 100$  m $^2$  s $^{-4}$ , the maximum error in  $U$  or  $V$  at any location was  $\approx 0.5\%$  of the true values, and the maximum error in  $v_r$  at any location or time was  $\approx 0.12$  m s $^{-1}$ , about  $0.34\%$  of the true peak value of  $v_r$  ( $\approx 35$  m s $^{-1}$ ).

We also ran a uniform translation test to explore the possibility of solution nonuniqueness. Following SWP10a and Shapiro et al. (2015), we note that if a tracer varies with wavelength  $\lambda$  in the  $y$  direction, and  $U_{\text{true}}$  and  $V_{\text{true}}$  are the true pattern-translation components, there are an infinite number of solutions  $U = U_{\text{true}}$ ,  $V = V_{\text{true}} + M\lambda/T$  ( $M$  is an integer,



TABLE 1. Experiments using AIR data from a band of heavy convective rainfall on 4 Sep 2018. Radial velocity data from the  $5.5^\circ$  elevation angle are supplied at  $\sim 2$  min intervals ( $t_i = 2202:53$  UTC,  $t_m = 2204:58$  UTC,  $t_f = 2207:03$  UTC). The analyzed radial velocity is compared to the AIR radial velocity at  $t_v = 2203:55$  UTC. An asterisk indicates a “ $K$  threshold” experiment in which the procedure did not converge but subsequently increasing  $K$  by  $0.001 \text{ m}^2 \text{ s}^{-4}$  did yield convergence. The Best Constant  $U, V$  run is the Specified Constant  $U, V$  run with the lowest RMSE (see Fig. 6).

Experiment	RMSE ( $\text{m s}^{-1}$ )	CC
Forward Persistence	1.237	0.941
Backward Persistence	1.090	0.955
Linear Time Interpolation	0.844	0.972
Best Constant $U, V$ run	0.521	0.985
Large- $K$ run ( $K = 1.0 \text{ m}^2 \text{ s}^{-4}$ )	0.544	0.982
$K = 0.1 \text{ m}^2 \text{ s}^{-4}$	0.544	0.982
$K = 0.01 \text{ m}^2 \text{ s}^{-4}$	0.542	0.982
$K = 0.005 \text{ m}^2 \text{ s}^{-4}$	0.543	0.983
$K = 0.002 \text{ m}^2 \text{ s}^{-4}$	0.505	0.987
$K = 0.001 \text{ m}^2 \text{ s}^{-4}$	0.501*	0.988*

$T$  is data input time interval) that satisfy the analysis constraints exactly. Associated with the first spurious modes  $M = \pm 1$  (with  $T = 180 \text{ s}$ ,  $\lambda = 10 \text{ km}$ ,  $V_{\text{true}} = 15 \text{ m s}^{-1}$ ) are the aliased solutions  $V \approx -40.56 \text{ m s}^{-1}$  and  $V \approx 70.56 \text{ m s}^{-1}$ . To retrieve the  $-40.56 \text{ m s}^{-1}$  aliased solution, we left the first guess for  $U$  at  $0 \text{ m s}^{-1}$ , but changed the first guess for  $V$  to  $-50 \text{ m s}^{-1}$ . In a test with  $K = 1 \text{ m}^2 \text{ s}^{-4}$ , the procedure converged with good precision to the aliased solution:  $U$  was nearly constant throughout the domain and close to its true value of  $5 \text{ m s}^{-1}$  ( $4.97 < U < 5.00 \text{ m s}^{-1}$ ), while  $V$  was nearly constant and close to the  $-40.56 \text{ m s}^{-1}$  aliased solution ( $-40.45 < V < -40.42 \text{ m s}^{-1}$ ).

Results from a solid body vortex test in which  $K = 0.0002 \text{ m}^2 \text{ s}^{-4}$  are shown in Fig. 4. As anticipated, the retrieved

$U, V$  fields are in qualitatively good agreement with the exact  $U, V$  fields in the interior of the domain, with larger errors—on the order of  $1 \text{ m s}^{-1}$ —in the vicinity of boundaries on which the true normal gradients are inconsistent with zero-normal gradient conditions (southern/northern boundaries for  $U$ , western/eastern boundaries for  $V$ ). Despite  $\sim 1 \text{ m s}^{-1}$  peak errors in  $U$  and  $V$ , the peak error in  $v_r$  at any point or time was only  $\approx 0.15 \text{ m s}^{-1}$ , or  $\approx 0.75\%$  of the true peak value of  $v_r$  which was  $\approx 20 \text{ m s}^{-1}$ . An additional experiment confirmed the amplitude principle for  $K$  described in section 5: doubling the amplitude of the radial velocity (taking  $A = 40 \text{ m s}^{-1}$ ) while increasing  $K$  by a factor of 4 (taking  $K = 0.0008 \text{ m}^2 \text{ s}^{-4}$ ) produced results that differed imperceptibly from those in the above experiment.

## 7. Tests using AIR data

The AIR is a mobile rapid-scan X-band phased array radar, designed, maintained, and operated by the Advanced Radar Research Center (ARRC) at the University of Oklahoma (Isom et al. 2013; Kurdzo et al. 2017; Mahre et al. 2018; Griffin et al. 2019). We conducted advection-correction tests using AIR data of heavy convective rainfall in a band of thunderstorms during the afternoon of 4 September 2018 near El Reno, Oklahoma, and of a decaying EF-2 rated tornado and its parent storm on 27 May 2015 near Canadian, Texas.

Radial velocity data were supplied to the analysis procedure at three data input times, with data at a fourth time level, a verification time  $t_v$  within analysis subwindow 1 ( $t_i < t_v < t_m$ ) used to assess the analysis performance. As the analysis (computational) time step  $\Delta t$  in our AIR tests was only 4 s, the sequence of analysis times within the analysis window was guaranteed to include an analysis time that closely matched the verification time (differing by no more than 2 s). Results are quantified using the RMSE,

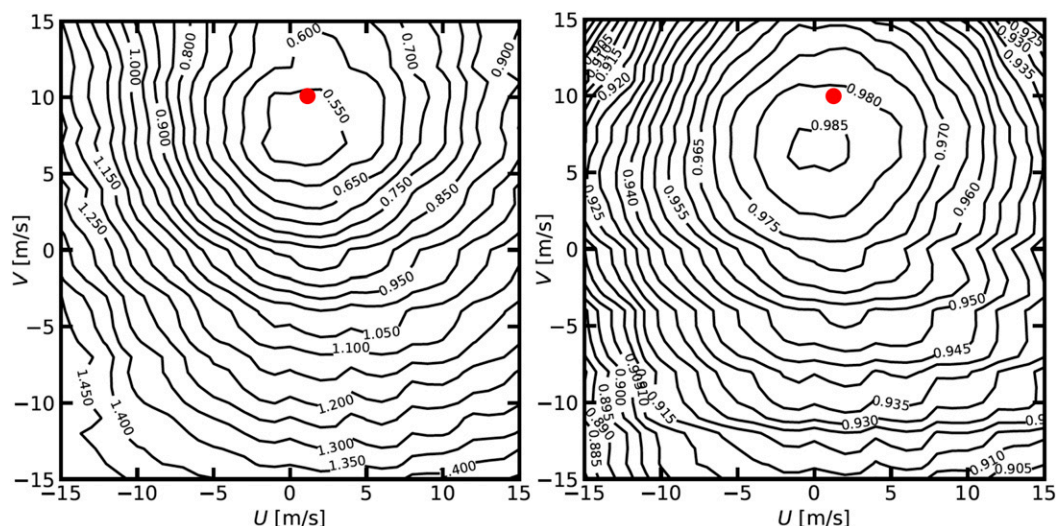


FIG. 6. (left) RMSE and (right) CC at the verification time  $t_v = 2203:55$  UTC 4 Sep 2018 from the Specified Constant  $U, V$  experiments. The Best Constant  $U, V$  run yields  $\text{RMSE} \approx 0.521 \text{ m s}^{-1}$  and  $\text{CC} \approx 0.985$ . The red dot marks results from the Large- $K$  run ( $K = 1 \text{ m}^2 \text{ s}^{-4}$ ), where  $U \approx 0.8 \text{ m s}^{-1}$ ,  $V \approx 10.2 \text{ m s}^{-1}$ .



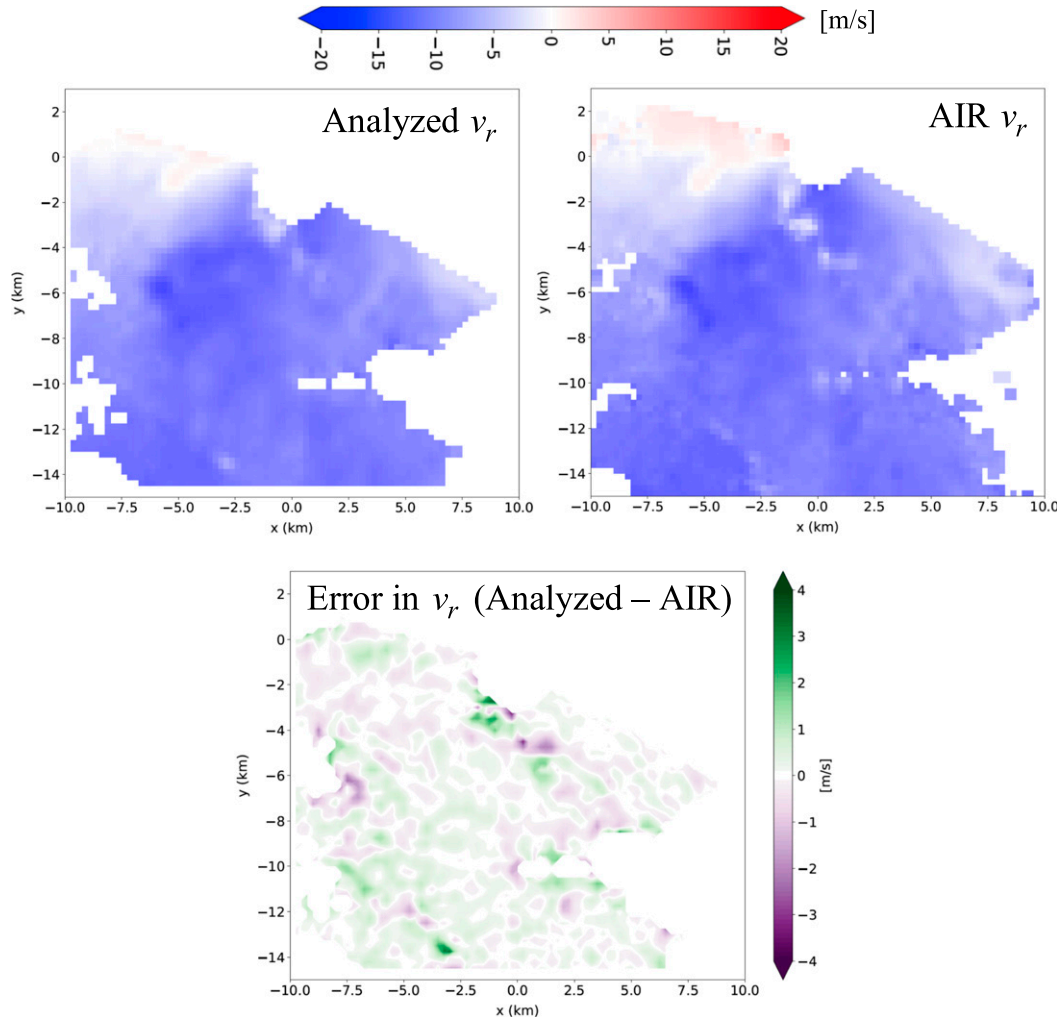


FIG. 7. (top left) Analyzed  $v_r$ , (top right) AIR  $v_r$ , and (bottom) error in analyzed  $v_r$  (analyzed  $v_r$  minus AIR  $v_r$ ) at the verification time  $t_v = 2203:55$  UTC 4 Sep 2018 from the advection correction experiment in which  $K = 0.002 \text{ m}^2 \text{ s}^{-4}$ . The AIR is at  $x = 0 \text{ km}$ ,  $y = 0 \text{ km}$ .

$$\text{RMSE} \equiv \sqrt{\frac{1}{P} \sum (X - Y)^2}, \quad (7.1)$$

and the correlation coefficient (CC),

$$\text{CC} \equiv \frac{\overline{XY} - \overline{X}\overline{Y}}{\sqrt{\overline{X^2} - \overline{X}^2} \sqrt{\overline{Y^2} - \overline{Y}^2}}. \quad (7.2)$$

Here,  $X$  and  $Y$  are the analyzed and observed  $v_r$  fields, respectively, at the verification time, the summations are over the  $P$  analysis points on which both analyzed and observed  $v_r$  fields are available, and an overbar denotes an average over those  $P$  points; that is, for a variable  $\phi$ ,  $\overline{\phi} \equiv (1/P) \sum \phi$ .

To put the analysis results in context, we also ran a suite of control experiments:

- 1) Forward Persistence: The  $v_r$  field analyzed at the verification time  $t_v$  is the  $v_r$  field observed at the initial time  $t_i$ . The

velocity field is treated as stationary—no attempt is made to account for advection.

- 2) Backward Persistence: This run is similar to the Forward Persistence run, but with the  $v_r$  field analyzed at the verification time  $t_v$  taken as the  $v_r$  field observed at the intermediate time  $t_m$ . Again, there is no advection-correction step.
- 3) Linear Time Interpolation: The  $v_r$  field is analyzed by linearly interpolating  $v_r$  data from the initial and intermediate times to the verification time. There is no advection-correction step.
- 4) Specified Constant  $U$ ,  $V$ : The  $v_r$  field is advection corrected, but with  $U$ ,  $V$  imposed as specified constants ( $U$  and  $V$  varied in  $1 \text{ m s}^{-1}$  increments from  $-15$  to  $15 \text{ m s}^{-1}$ ) rather than derived from (5.1) and (5.2). Of these  $31^2 = 961$  experiments, the one yielding the smallest RMSE is referred to as the Best Constant  $U$ ,  $V$  experiment.

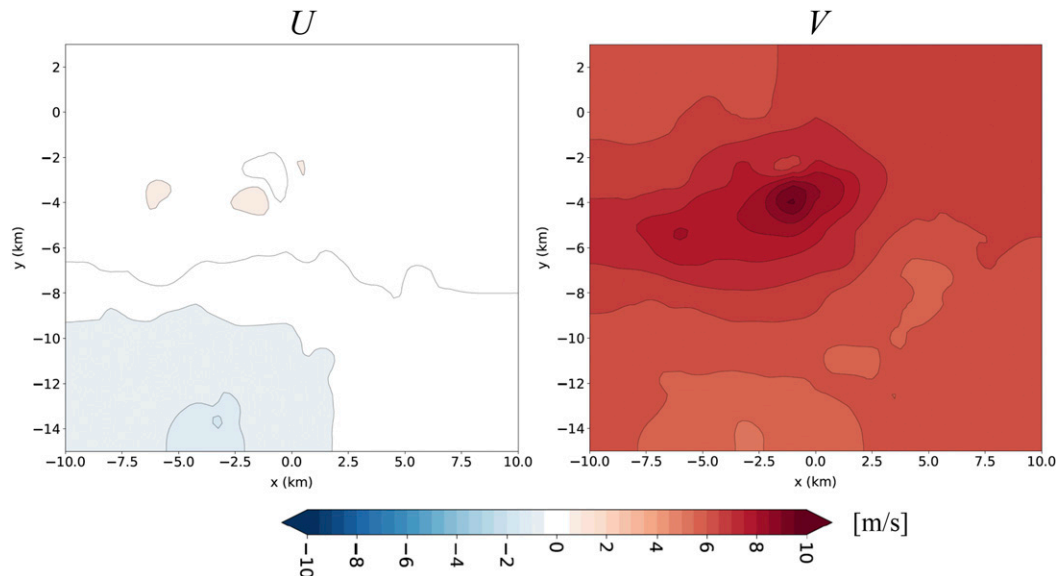


FIG. 8. Pattern-translation components (left)  $U$  and (right)  $V$  from a 4 Sep 2018 experiment in which  $K = 0.002 \text{ m}^2 \text{ s}^{-4}$ .

5) Large  $K$ : The  $v_r$  field at the verification time is obtained from the full advection correction procedure, but with the smoothness constant  $K$  set to a value so large that the retrieved  $U$ ,  $V$  fields are nearly constant. This run mimics the  $v_r$ -based Gal-Chen (1982) procedure.

In both the 4 September 2018 and 27 May 2015 deployments, the AIR was steered mechanically in azimuth, while transmitting a fan beam  $20^\circ$  wide in elevation and  $1^\circ$  wide in azimuth. For each pulse, data received by the AIR’s multielement antenna array were postprocessed using digital beamforming (Kurdzo et al. 2014). For both cases, the temporal resolution of the data was 10 s. The scan mode employed pulse compression with a  $5.25\text{-}\mu\text{s}$  pulse, yielding a native range resolution of 37.5 m (Kurdzo et al. 2014, 2017). AIR data were oversampled to 30 m in range and  $0.5^\circ$  resolution in both azimuth and elevation (factor-of-2 oversampling). Radial velocities from 27 May 2015 were dealiased using Solo II software (Oye et al. 1995), with questionable values removed manually. A ground-clutter filter (Siggia and Passarelli 2004; Cho and Chornoboy 2005) was applied to the 4 September 2018 data. No dealiasing was needed for the 4 September 2018 case, and no ground-clutter filter was needed for the 27 May 2015 case. More details about the 27 May 2015 dataset can be found in Griffin et al. (2019).

AIR data were interpolated to a 2D Cartesian analysis grid on a constant elevation angle surface with a uniform grid spacing ( $\Delta x = \Delta y = 250 \text{ m}$ ) using a Cressman filter (Cressman 1959) with 400-m radius of influence. Experiments with 4 September data were conducted on the  $5.5^\circ$  elevation surface because that surface had the most extensive data coverage. Experiments with 27 May data were conducted on the  $4^\circ$  elevation surface because that level was within a layer of good data coverage, tornado strength decreased with height above that surface, and tornado size decreased (albeit slightly) beneath that surface. We report on experiments for which data

are input at  $\sim 2 \text{ min}$  intervals, and the verification time is halfway between the initial and intermediate data input times. The radial velocity fields at the three data input times are shown for both cases in Fig. 5. The tornado appears in the 27 May data as a dipole-like feature in the radial velocity field centered on a point near  $x = -5 \text{ km}$ ,  $y = 3 \text{ km}$ . It is strongest at the initial time. Even away from the tornado, the winds in the 27 May case are generally stronger and more variable than in the 4 September case.

For each dataset, we determined a threshold value of  $K$  at and beneath which the procedure did not converge,

TABLE 2. Experiments using AIR data from a decaying tornado and its parent storm on 27 May 2015. Radial velocity data from the  $4.0^\circ$  elevation angle are supplied at  $\sim 2 \text{ min}$  intervals ( $t_i = 2203:52 \text{ UTC}$ ,  $t_m = 2206:01 \text{ UTC}$ ,  $t_f = 2207:59 \text{ UTC}$ ). The analyzed radial velocity is compared to the AIR radial velocity at  $t_v = 2204:56 \text{ UTC}$ . An asterisk indicates a “ $K$  threshold” experiment in which the procedure did not converge but subsequently increasing  $K$  by  $0.001 \text{ m}^2 \text{ s}^{-4}$  did yield convergence. The Best Constant  $U$ ,  $V$  run is the Specified Constant  $U$ ,  $V$  run with the lowest RMSE (see Fig. 9).

Experiment	RMSE ( $\text{m s}^{-1}$ )	CC
Forward Persistence	2.889	0.861
Backward Persistence	2.729	0.859
Linear Time Interpolation	1.789	0.941
Best Constant $U$ , $V$ run	1.696	0.948
Large- $K$ run ( $K = 10.0 \text{ m}^2 \text{ s}^{-4}$ )	1.797	0.942
$K = 1.0 \text{ m}^2 \text{ s}^{-4}$	1.774	0.944
$K = 0.1 \text{ m}^2 \text{ s}^{-4}$	1.652	0.951
$K = 0.01 \text{ m}^2 \text{ s}^{-4}$	1.450	0.961
$K = 0.005 \text{ m}^2 \text{ s}^{-4}$	1.428	0.962
$K = 0.003 \text{ m}^2 \text{ s}^{-4}$	1.414	0.964
$K = 0.002 \text{ m}^2 \text{ s}^{-4}$	1.405*	0.964*

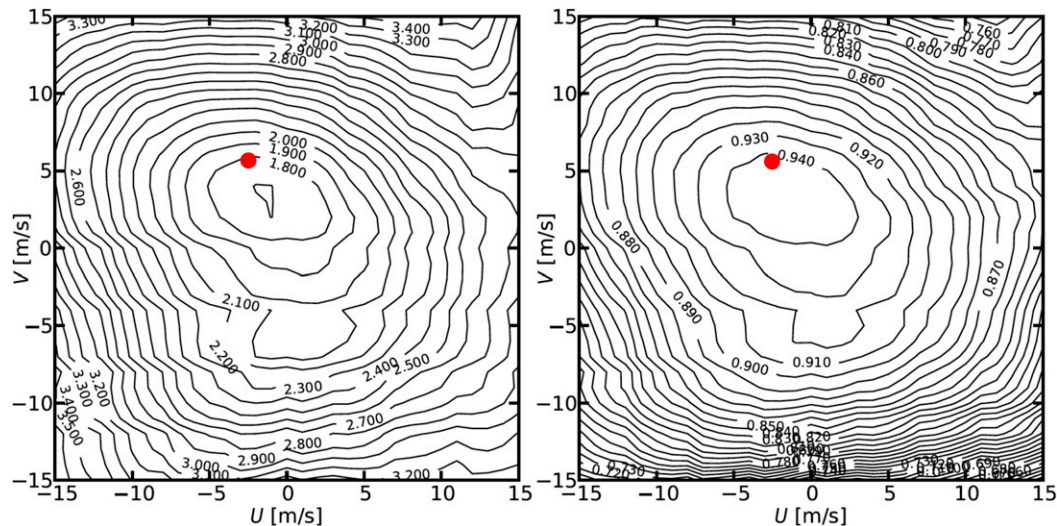


FIG. 9. (left) RMSE and (right) CC at the verification time  $t_v = 2204:56$  UTC 27 May 2015 from the Specified Constant  $U, V$  runs. The Best Constant  $U, V$  run yields  $\text{RMSE} \approx 1.696 \text{ m s}^{-1}$  and  $\text{CC} \approx 0.948$ . The red dot marks results from the Large- $K$  run ( $K = 10 \text{ m}^2 \text{ s}^{-4}$ ), where  $U \approx -3.2 \text{ m s}^{-1}$ ,  $V \approx 5.7 \text{ m s}^{-1}$ .

but subsequently increasing  $K$  by  $0.001 \text{ m}^2 \text{ s}^{-4}$  did yield convergence. The nonconvergence in these threshold experiments was associated with a small-amplitude “cycling” of  $U, V$  iterates around unchanging values, with only slight changes to  $v_r$  from one iteration level to the next.

Statistics from tests with the 4 September data are summarized in Table 1. The best of the advection-correction experiments had lower RMSE and higher CC than any of the non-advection-correction experiments, with the RMSE in the two persistence experiments being more than twice as large as the RMSE in any of the advection-correction experiments. The RMSE generally decreased with decreasing  $K$ , and was lowest in the  $K$  threshold run ( $K = 0.001 \text{ m}^2 \text{ s}^{-4}$ ). Statistics from the Specified Constant  $U, V$  runs and a Large- $K$  run are shown in Fig. 6. The RMSE in the Large- $K$  run was similar to but somewhat larger than in the Best Constant  $U, V$  experiment, while the RMSE in the runs with the smaller values of  $K$  were less than the RMSE in the Best Constant  $U, V$  runs. The analyzed  $v_r$ , AIR  $v_r$ , and error-in- $v_r$  fields in the  $K = 0.002 \text{ m}^2 \text{ s}^{-4}$  run are presented in Fig. 7. The corresponding  $U, V$  fields are shown in Fig. 8. The dominant northward translation evident in Fig. 8 is consistent with the motion seen in animations of the reflectivity field and our perception of cloud motions during the field deployment. The error-in- $v_r$  field (lower panel of Fig. 7) appears to contain both amplitude and phase errors. A peak error of almost  $3.7 \text{ m s}^{-1}$  is found near the point  $x = -1.0 \text{ km}$ ,  $y = -2.5 \text{ km}$ , in a lobe of relatively weak radial velocities.

Results from the 27 May case are summarized in Table 2. As in the tests with 4 September data, the best of the 27 May advection-correction experiments had lower RMSE and higher CC than any of the non-advection-correction experiments. Again, the RMSE decreased with decreasing  $K$ , and was lowest in the  $K$  threshold run ( $K = 0.002 \text{ m}^2 \text{ s}^{-4}$ ). Statistics from the Specified Constant  $U, V$  runs and the Large- $K$  run are shown in

Fig. 9. As in the 4 September case, errors in the Large- $K$  run were similar to but somewhat larger than in the Best Constant  $U, V$  run, while the RMSE in the runs with the smaller values of  $K$  were less than the RMSE in the Best Constant  $U, V$  run. The analyzed  $v_r$ , AIR  $v_r$ , and error-in- $v_r$  fields in the  $K = 0.005 \text{ m}^2 \text{ s}^{-4}$  run are shown in Fig. 10. The corresponding  $U, V$  fields are shown in Fig. 11. Although the errors in  $v_r$  tend to be somewhat larger near the tornado than in many other locations, the largest error ( $\approx 8.7 \text{ m s}^{-1}$ ) is far from the tornado, near a point ( $x = -17.5 \text{ km}$ ,  $y = 4.5 \text{ km}$ ) on the northern flank of a lobe of negative radial velocities (blue blob). At this location, the AIR  $v_r$  is negative, with a magnitude of a few meters per second, while the analyzed  $v_r$  is positive and of similar magnitude. This error might be a phase error enhanced by evolution effects not properly accounted for by the procedure (size of blue blob is too small in the analysis).

Tables 1 and 2 show that the value of  $K$  used in the 27 May Large- $K$  run is 10 times larger than in the 4 September Large- $K$  run. We settled on these  $K$  values because they produced similar (small) spatial changes to  $U$  and  $V$  in both datasets, with peak domain-wide variations of  $\approx 0.05 \text{ m s}^{-1}$ . Additionally, the threshold for  $K$  at and beneath which the procedure did not converge was about twice as large in the 27 May case than in the 4 September case. Despite their failure to converge, these threshold tests produced the lowest RMSE and largest CC for both datasets. The relatively larger values of  $K$  in the Large- $K$  and threshold runs in the 27 May case compared to the 4 September case are qualitatively consistent with the amplitude principle for  $K$  discussed in section 5. In additional tests in which  $K$  was beneath its threshold value and further decreased, the amplitude of the  $U, V$ -iteration cycle increased, and the procedure eventually became unstable.

The analytical and real data tests described herein were obtained with parameter settings that had not been optimized for computational efficiency. Additional tests using AIR data

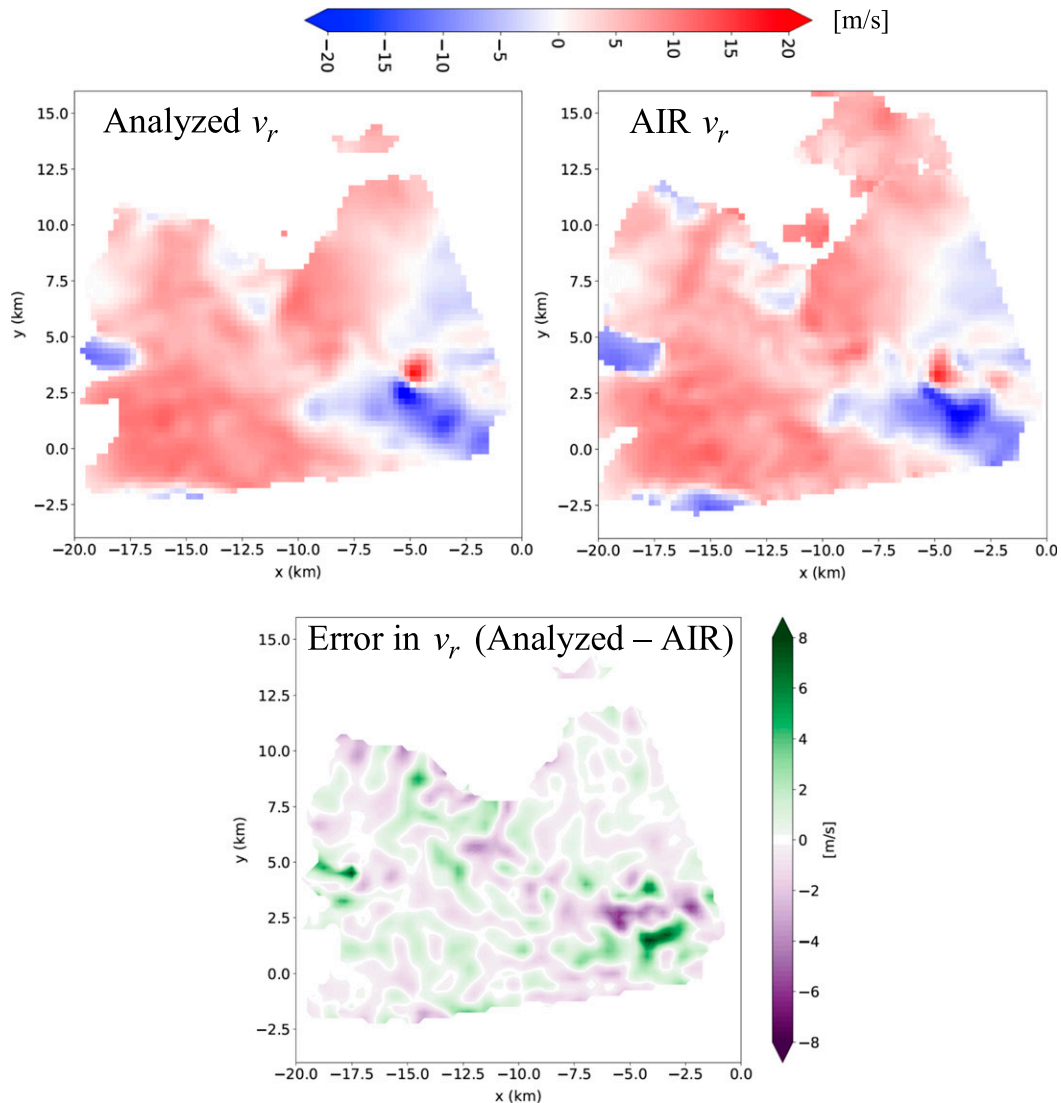


FIG. 10. (top left) Analyzed  $v_r$ , (top right) AIR  $v_r$ , and (bottom) error in analyzed  $v_r$  (analyzed  $v_r$  minus AIR  $v_r$ ) at the verification time  $t_v = 2204:56$  UTC 27 May 2015 from the advection correction experiment in which  $K = 0.005 \text{ m}^2 \text{ s}^{-4}$ . The AIR is at  $x = 0 \text{ km}$ ,  $y = 0 \text{ km}$ .

(not shown) showed that a significant speedup could be achieved simply by increasing the tolerance (TolOUT) for convergence of  $U$  and  $V$  in the outer loop. However, to prevent the procedure from converging prematurely in that loop—which could substantially increase analysis errors—the blending parameter  $wgt$  in (5.4) should be increased in tandem with the increase in TolOUT. When the original 27 May analysis using  $K = 0.005 \text{ m}^2 \text{ s}^{-4}$  was rerun with TolOUT increased a hundredfold to  $0.1 \text{ m s}^{-1}$  and  $wgt$  increased tenfold to 0.25, the execution time decreased from 112 to 3 min. Similarly, when the original 4 September analysis using  $K = 0.002 \text{ m}^2 \text{ s}^{-4}$  was rerun using these same increased parameters, the execution time decreased from 87 to 5 min. In both sped-up runs, the increase in RMSE ( $\Delta\text{RMSE}$ ) over the RMSE in the corresponding original run was negligible ( $\Delta\text{RMSE} \approx 0.007 \text{ m s}^{-1}$

for the 27 May analysis and  $\approx 0.002 \text{ m s}^{-1}$  for the 4 September analysis). Similar speedups were achieved by setting TolOUT to  $0.1 \text{ m s}^{-1}$  without changing  $wgt$ , but at the expense of a much larger  $\Delta\text{RMSE}$  ( $\Delta\text{RMSE} \approx 0.174 \text{ m s}^{-1}$  for the 27 May analysis and  $\approx 0.324 \text{ m s}^{-1}$  for the 4 September analysis).

## 8. Conclusions

A procedure to advection correct (analyze) the Doppler radial velocity field using spatially variable pattern-translation components ( $U$  and  $V$ ) is developed, with encouraging results obtained in proof-of-concept tests using data from the Atmospheric Imaging Radar (AIR). The advection-correction procedure is based on the minimization of a cost function that accumulates errors in a second-derivative frozen-turbulence constraint on the



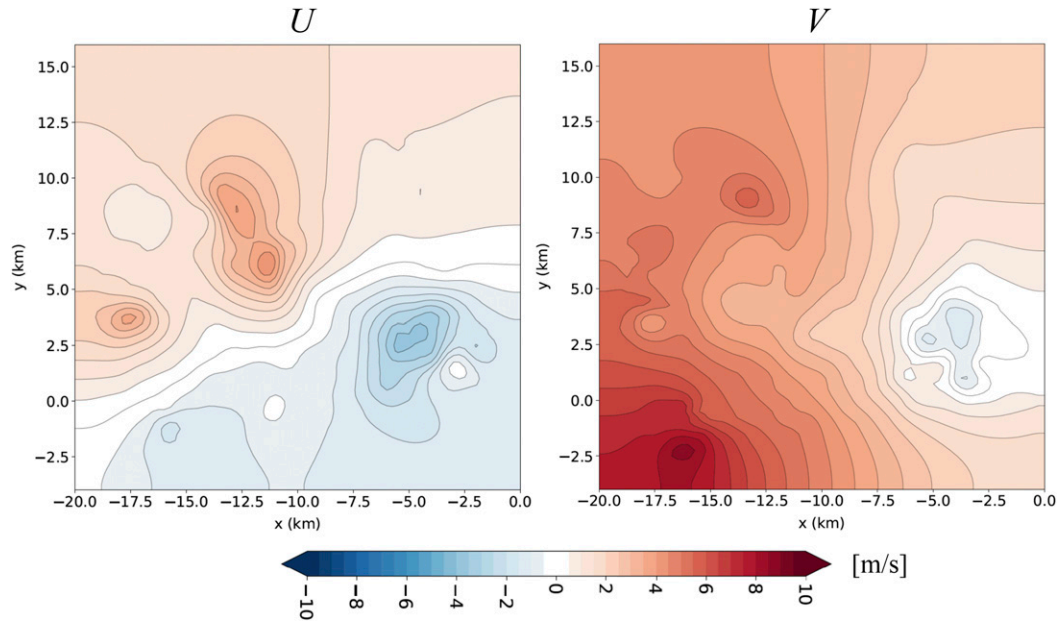


FIG. 11. Pattern-translation components (left)  $U$  and (right)  $V$  from a 27 May 2015 experiment in which  $K = 0.005 \text{ m}^2 \text{ s}^{-4}$ .

radial velocity field, while penalizing spatial gradients in  $U$  and  $V$ . The radial velocity field and associated  $U$ ,  $V$  fields are analyzed together as the iterative solution of the Euler–Lagrange equations arising from the minimization of the cost function. Radial velocities from three data input times are incorporated into the analysis. As in many advection-correction techniques that use the reflectivity field as a tracer, the new radial-velocity-based technique may be subject to solution nonuniqueness associated with temporal aliasing. Solution nonuniqueness was demonstrated in an analytical test in which the first guesses for  $U$  and  $V$  were set close to values associated with a spurious solution, but did not appear to be an issue in the AIR data tests.

After performing verification tests using analytical data, we conducted experiments using AIR data from a convective rainband on 4 September 2018 and a decaying tornado and its parent storm on 27 May 2015. In these AIR data tests, the procedure yielded radial velocities with lower RMSE and higher CC than radial velocities analyzed in any of the control runs (Forward Persistence, Backward Persistence, Linear Time Interpolation, Specified Constant  $U$ ,  $V$ , and Large  $K$ ).

The procedure is sensitive to the value of a smoothness parameter ( $K$ ). In AIR data tests spanning three orders of magnitude of  $K$ , the best results were obtained with relatively small values of  $K$ , though for values not much smaller than these, the procedure became unstable. For relatively large  $K$ , the retrieved  $U$ ,  $V$  fields were nearly constant, and the errors in the analyzed radial velocity field were similar to (though slightly worse than) those from the Best Constant  $U$ ,  $V$  experiment. As the procedure lacks an objective method to determine appropriate values of  $K$ , we recommend that such values be explored on a case-by-case basis, using trial and error, perhaps guided by visual estimates of physically reasonable  $U$ ,  $V$  fields from animations of the data.

The stability and execution time of the procedure are sensitive to computational parameters such as the convergence thresholds (tolerances) for  $U$  and  $V$  on the inner and outer iteration loops and an underrelaxation (blending) parameter used to weight the updated and previous iterates on the outer loop. Experimentation may also help determine appropriate values of these parameters on a case-by-case basis.

The primary utility of the new procedure is to the analysis of nonsimultaneously collected radial velocity data from two or more radars to common analysis times for use in multiple-Doppler wind syntheses of severe convective phenomena. Since some experimentation is required to establish appropriate smoothing and computational parameter values or to explore the threat of solution nonuniqueness, the procedure is currently more suitable for non-real-time research applications than use in an operational analysis or data assimilation setting. Future work will focus on determining procedures to estimate some of these parameters objectively.

**Acknowledgments.** This research was supported by the National Science Foundation (NSF) under Grant AGS-1623626. Data collection and analysis of the 27 May 2015 case were supported by NSF AGS-1303685 and AGS-1823478; Jim Kurdzo led the deployment, Javier Lujan assisted with the data collection, and Casey Griffin dealiased and quality controlled the data. The AIR is maintained and operated by the Advanced Radar Research Center (ARRC) of the University of Oklahoma. We are grateful to the ARRC engineering staff for their support of our radar experiments. Shawn Riley provided computing assistance. The authors thank Lou Wicker, Qin Xu, Nikola Petrov, and the anonymous referees for their helpful comments.



**Data availability statement.** The AIR data and Fortran code used to generate the analyses reported on herein are available from the corresponding author upon request.

## APPENDIX A

### Analysis Using Two Time Levels of Data

If  $v_r$  data are only available at two data input times, then (3.11) and the equivalent system (3.12)–(3.14) apply throughout the analysis window, and (3.18a) and (3.18b) are replaced by the single equation  $\Theta = (A_1 t + B_1)E_1(t)$ . In view of (3.10a), (3.10b), and (3.12),  $A_1 = B_1 = 0$ , so  $D^2\Gamma/Dt^2$  is identically zero. Equations (3.12) and (3.13) then show that  $\Theta$  and  $\Psi$  are identically zero, and (4.8) and (4.9) reduce to Laplace's equations for  $U$  and  $V$ , the solutions of which [subject to the zero-normal-gradient conditions (4.2a), (4.2b) and (4.10a), (4.10b)] are arbitrary constants, with no links to the  $v_r$  field. Such an analysis has no practical value.

## APPENDIX B

### Analysis Using an Arbitrary Number of Time Levels of Data

To incorporate data from an arbitrary number  $n$  of input times, the analysis window should include  $n - 2$  intermediate data input times and  $n - 1$  analysis subwindows. The solution of (3.11) [analog of (3.20a) and (3.20b)] then contains  $4(n - 1)$  integration constants, which satisfy  $4(n - 1)$  linear algebraic equations: 1 equation from imposing data at the initial time, 1 equation from imposing data at the end time,  $2(n - 2)$  equations from imposing data at the intermediate data input times (as in the  $n = 3$  case, data at each intermediate data input time are used twice), 2 equations from (3.10a), (3.10b), and  $2(n - 2)$  equations expressing continuity of  $D\Gamma/Dt$  and  $D^2\Gamma/Dt^2$  at the intermediate data input times. The integration constants can thus be obtained by solving  $4(n - 1)$  linear algebraic equations.  $U$  and  $V$  then follow as solutions of (4.8) and (4.9) subject to boundary conditions (4.2a), (4.2b) and (4.10a), (4.10b).

## APPENDIX C

### Classification of (4.8) and (4.9) for $U$ and $V$

The classification of (4.8) and (4.9) is complicated by the presence of  $\Psi$  in the integrals on the right-hand sides of those equations. The first term in the definition (3.13) of  $\Psi$  is  $D\Theta/Dt$  which, in view of (3.12), is  $D^3\Gamma/Dt^3$ . The expansion of that term, facilitated by (2.2), generates second derivative terms in  $U$  and  $V$ . The classification of (4.8) is based only on the second derivative terms in  $U$ . These terms collect together as

$$A \frac{\partial^2 U}{\partial x^2} + 2B \frac{\partial^2 U}{\partial x \partial y} + C \frac{\partial^2 U}{\partial y^2}, \quad (\text{C.1})$$

where

$$A \equiv 1 + \gamma U^2, \quad B \equiv \gamma UV, \quad C \equiv 1 + \gamma V^2, \quad (\text{C.2})$$

and

$$\gamma \equiv \frac{1/\kappa}{t_f - t_i} \int_{t_i}^{t_f} \alpha(\Gamma_x)^2 dt. \quad (\text{C.3})$$

The second-order quasi-linear operator (C.1) is classified using the same procedure as for linear operators (Garabedian 1998). Since  $\kappa$ ,  $\alpha$ ,  $t_f - t_i$ , and  $(\Gamma_x)^2$  are nonnegative, (C.3) shows that  $\gamma$  is nonnegative. Equations (C.2) then show that  $A$ ,  $C$ , and  $AC - B^2$  are strictly positive for all  $U$  and  $V$ , so (C.1) is an elliptic operator. Similarly, it can be shown that the operator analogous to (C.1) arising from (4.9) is elliptic.

## APPENDIX D

### Comment on the Forcing Terms in (4.8) and (4.9)

The simplest treatment of the right-hand sides of (4.8) and (4.9) within the (outer) iterative framework would be to express them in terms of variables from the previous iteration level. We would then consider (4.8) as the Poisson-like equation,

$$\nabla \cdot (\kappa \nabla U^{N+1}) = Q^N, \quad (\text{D.1})$$

where

$$Q^N \equiv \frac{1}{t_f - t_i} \int_{t_i}^{t_f} \alpha^N \left[ \Theta^N \frac{\partial}{\partial x} \left( \frac{D\Gamma}{Dt} \right)^N - \Gamma_x^N \Psi^N \right] dt, \quad (\text{D.2})$$

and a superscript denotes the iteration level. Integrating (D.1) over the analysis domain, and applying the divergence theorem to the left-hand side yields

$$\int \kappa \left( \frac{\partial U}{\partial n} \right)^{N+1} dl = \iint Q^N dx dy, \quad (\text{D.3})$$

where the left-hand side of (D.3) is a boundary integral, and  $\partial/\partial n$  is a normal derivative. In view of (4.2a) and (4.2b), the boundary integral is zero, and (D.3) yields the compatibility condition,

$$\iint Q^N dx dy = 0. \quad (\text{D.4})$$

As there are no restrictions on  $Q^N$  that would make its integral vanish, (D.4) will generally be violated, and no solution for  $U^{N+1}$  exists.

Next, consider an iterative framework in which (4.8) and (4.9) are written as (5.1) and (5.2), respectively, with  $U$ ,  $V$  treated as valid at the  $(N + 1)$ th iteration level, and  $a$ ,  $b$ ,  $c$ ,  $e$ ,  $g$  as valid at the  $N$ th iteration level (superscripts omitted). In this framework, integration of (5.1) and (5.2) yields compatibility conditions that are not generally violated. We do not examine solution existence further, but use the energy method (Gustafson 1987) to show that if a solution exists, it is unique. We denote by  $U_1$ ,  $V_1$  the real variables satisfying (5.1),

(5.2) with boundary conditions (4.2a), (4.2b), (4.10a), (4.10b), and explore whether a second set of real variables,  $U_2$ ,  $V_2$ , can satisfy the same equations and boundary conditions (these subscripts are not related to the subscripts 1 and 2 used in section 3 to denote analysis subwindows). Subtracting the forms of (5.1), (5.2) applied to  $U_1$ ,  $V_1$  from those applied to  $U_2$ ,  $V_2$  shows that the difference functions  $U_d \equiv U_2 - U_1$ ,  $V_d \equiv V_2 - V_1$  satisfy

$$\frac{\partial^2 U_d}{\partial x^2} + \frac{\partial^2 U_d}{\partial y^2} + \frac{1}{\kappa} \frac{\partial \kappa}{\partial x} \frac{\partial U_d}{\partial x} + \frac{1}{\kappa} \frac{\partial \kappa}{\partial y} \frac{\partial U_d}{\partial y} = bU_d + cV_d, \quad (\text{D.5})$$

$$\frac{\partial^2 V_d}{\partial x^2} + \frac{\partial^2 V_d}{\partial y^2} + \frac{1}{\kappa} \frac{\partial \kappa}{\partial x} \frac{\partial V_d}{\partial x} + \frac{1}{\kappa} \frac{\partial \kappa}{\partial y} \frac{\partial V_d}{\partial y} = cU_d + gV_d. \quad (\text{D.6})$$

Subtracting the form of (4.2a) and (4.2b) applied to  $U_1$  from that applied to  $U_2$ , and subtracting the form of (4.10a) and (4.10b) applied to  $V_1$  from that applied to  $V_2$  yields

$$\frac{\partial U_d}{\partial n} = 0, \quad \frac{\partial V_d}{\partial n} = 0 \text{ on boundaries.} \quad (\text{D.7})$$

Adding  $\kappa U_d \times (\text{D.5})$  to  $\kappa V_d \times (\text{D.6})$ , and rearranging the result produces

$$\nabla \cdot (\kappa U_d \nabla U_d + \kappa V_d \nabla V_d) = \kappa(|\nabla U_d|^2 + |\nabla V_d|^2 + bU_d^2 + 2cU_d V_d + gV_d^2). \quad (\text{D.8})$$

When (D.8) is integrated over the analysis domain, the left-hand side vanishes [application of the divergence theorem yields a boundary integral that vanishes because of (D.7)], leaving

$$\iint \kappa(|\nabla U_d|^2 + |\nabla V_d|^2 + bU_d^2 + 2cU_d V_d + gV_d^2) dx dy = 0. \quad (\text{D.9})$$

To show that the integrand in (D.9) is nonnegative [clearly its first two terms are nonnegative], apply Schwarz's inequality (Rudin 1976) to  $\sqrt{\alpha} \partial/\partial x D\Gamma/Dt$  and  $\sqrt{\alpha} \partial/\partial y D\Gamma/Dt$ , obtaining

$$\left[ \int_{t_i}^{t_f} \left( \sqrt{\alpha} \frac{\partial}{\partial x} \frac{D\Gamma}{Dt} \right) \left( \sqrt{\alpha} \frac{\partial}{\partial y} \frac{D\Gamma}{Dt} \right) dt \right]^2 \leq \int_{t_i}^{t_f} \left( \sqrt{\alpha} \frac{\partial}{\partial x} \frac{D\Gamma}{Dt} \right)^2 dt \int_{t_i}^{t_f} \left( \sqrt{\alpha} \frac{\partial}{\partial y} \frac{D\Gamma}{Dt} \right)^2 dt. \quad (\text{D.10})$$

From (5.3b), (5.3c), and (5.3e), we see that (D.10) is equivalent to  $c^2 \leq bg$  or, since  $b$  and  $g$  are nonnegative,

$$c + \sqrt{bg} \geq 0, \quad (\text{D.11a})$$

and

$$c - \sqrt{bg} \leq 0. \quad (\text{D.11b})$$

Next, write the sum of the last three terms in (D.9) in the alternative forms,

$$bU_d^2 + 2cU_d V_d + gV_d^2 = (\sqrt{b}U_d + \sqrt{g}V_d)^2 + 2(c - \sqrt{bg})U_d V_d, \quad (\text{D.12})$$

and

$$bU_d^2 + 2cU_d V_d + gV_d^2 = (\sqrt{b}U_d - \sqrt{g}V_d)^2 + 2(c + \sqrt{bg})U_d V_d. \quad (\text{D.13})$$

The first (squared) terms on the right-hand sides of (D.12) and (D.13) are nonnegative. If  $U_d V_d \geq 0$ , then (D.11a) shows that the last term of (D.13) is nonnegative, while if  $U_d V_d \leq 0$ , (D.11b) shows that the last term of (D.12) is nonnegative. In either case,

$$bU_d^2 + 2cU_d V_d + gV_d^2 \geq 0, \quad (\text{D.14})$$

and the integrand in (D.9) is nonnegative.

If  $|\nabla U_d|^2$ ,  $|\nabla V_d|^2$ , or  $bU_d^2 + 2cU_d V_d + gV_d^2$  are positive anywhere then, in view of (D.14), (D.9) would be violated. Thus,  $|\nabla U_d|^2$  and  $|\nabla V_d|^2$  must vanish [so  $U_d$ ,  $V_d$  are constants, and (D.7) is satisfied], and

$$bU_d^2 + 2cU_d V_d + gV_d^2 = 0. \quad (\text{D.15})$$

As the discriminant  $c^2 - bg$  in the quadratic formula solution of (D.15) for  $U_d$  as a function of  $V_d$  is negative ( $c^2 \leq bg$ ),  $U_d$  is imaginary if  $V_d$  is real. However, since  $U_d$  and  $V_d$  should be real, we must have  $U_d = V_d = 0$  ( $U_2 = U_1$ ,  $V_2 = V_1$ ), and the solution is unique.

## REFERENCES

- Anagnostou, E. N., and W. F. Krajewski, 1999: Real-time radar rainfall estimation. Part I: Algorithm formulation. *J. Atmos. Oceanic Technol.*, **16**, 189–197, [https://doi.org/10.1175/1520-0426\(1999\)016<0189:RTRREP>2.0.CO;2](https://doi.org/10.1175/1520-0426(1999)016<0189:RTRREP>2.0.CO;2).
- Austin, P. M., 1987: Relation between measured radar reflectivity and surface rainfall. *Mon. Wea. Rev.*, **115**, 1053–1070, [https://doi.org/10.1175/1520-0493\(1987\)115<1053:RBMRRR>2.0.CO;2](https://doi.org/10.1175/1520-0493(1987)115<1053:RBMRRR>2.0.CO;2).
- Bellon, A., and I. Zawadzki, 1994: Forecasting of hourly accumulations of precipitation by optimal extrapolation of radar maps. *J. Hydrol.*, **157**, 211–233, [https://doi.org/10.1016/0022-1694\(94\)90106-6](https://doi.org/10.1016/0022-1694(94)90106-6).
- Bousquet, O., P. Tabary, and J. Parent du Châtelet, 2007: On the value of operationally synthesized multiple-Doppler wind fields. *Geophys. Res. Lett.*, **34**, L22813, <https://doi.org/10.1029/2007GL030464>.
- Brown, R. A., R. M. Steadham, B. A. Flickinger, R. R. Lee, D. Sirmans, and V. T. Wood, 2005: New WSR-88D volume coverage pattern 12: Results of field tests. *Wea. Forecasting*, **20**, 385–393, <https://doi.org/10.1175/WAF848.1>.
- Burghlelea, T., E. Segre, and V. Steinberg, 2005: Validity of the Taylor hypothesis in a random spatially smooth flow. *Phys. Fluids*, **17**, 103101, <https://doi.org/10.1063/1.2077367>.
- Carbone, R. E., 1982: A severe frontal rainband. Part I: Stormwide hydrodynamic structure. *J. Atmos. Sci.*, **39**, 258–279, [https://doi.org/10.1175/1520-0469\(1982\)039<0258:ASFRPI>2.0.CO;2](https://doi.org/10.1175/1520-0469(1982)039<0258:ASFRPI>2.0.CO;2).

- Castro, J. J., A. A. Carsteanu, and J. D. Fuentes, 2011: On the phenomenology underlying Taylor's hypothesis in atmospheric turbulence. *Rev. Mex. Fis.*, **57**, 60–64.
- Cho, J. Y. N., and E. S. Chornoboy, 2005: Multi-PRI signal processing for the terminal Doppler weather radar. Part I: Clutter filtering. *J. Atmos. Oceanic Technol.*, **22**, 575–582, <https://doi.org/10.1175/JTECH1730.1>.
- Chong, M., J. Testud, and F. Roux, 1983: Three-dimensional wind field analysis from dual-Doppler radar data. Part II: Minimizing the error due to temporal variation. *J. Climate Appl. Meteor.*, **22**, 1216–1226, [https://doi.org/10.1175/1520-0450\(1983\)022<1216:TDWFAF>2.0.CO;2](https://doi.org/10.1175/1520-0450(1983)022<1216:TDWFAF>2.0.CO;2).
- Clark, T. L., F. I. Harris, and C. G. Mohr, 1980: Errors in wind fields derived from multiple-Doppler radars: Random errors and temporal errors associated with advection and evolution. *J. Appl. Meteor.*, **19**, 1273–1284, [https://doi.org/10.1175/1520-0450\(1980\)019<1273:EIWFDF>2.0.CO;2](https://doi.org/10.1175/1520-0450(1980)019<1273:EIWFDF>2.0.CO;2).
- Cressman, G. P., 1959: An operational objective analysis system. *Mon. Wea. Rev.*, **87**, 367–374, [https://doi.org/10.1175/1520-0493\(1959\)087<0367:AOOAS>2.0.CO;2](https://doi.org/10.1175/1520-0493(1959)087<0367:AOOAS>2.0.CO;2).
- Creutin, J.-D., E. Leblois, and J.-M. Lepioufle, 2015: Unfreezing Taylor's hypothesis for precipitation. *J. Hydrometeorol.*, **16**, 2443–2462, <https://doi.org/10.1175/JHM-D-14-0120.1>.
- Dennis, D. J. C., and T. B. Nickels, 2008: On the limitations of Taylor's hypothesis in constructing long structures in a turbulent boundary layer. *J. Fluid Mech.*, **614**, 197–206, <https://doi.org/10.1017/S0022112008003352>.
- Dowell, D. C., and H. B. Bluestein, 1997: The Arcadia, Oklahoma, storm of 17 May 1981: Analysis of a supercell during tornadogenesis. *Mon. Wea. Rev.*, **125**, 2562–2582, [https://doi.org/10.1175/1520-0493\(1997\)125<2562:TAOSOM>2.0.CO;2](https://doi.org/10.1175/1520-0493(1997)125<2562:TAOSOM>2.0.CO;2).
- Els golc, L. E., 1961: *Calculus of Variations*. Pergamon Press, 178 pp.
- Fabry, F., A. Bellon, M. R. Duncan, and G. L. Austin, 1994: High resolution rainfall measurements by radar for very small basins: The sampling problem reexamined. *J. Hydrol.*, **161**, 415–428, [https://doi.org/10.1016/0022-1694\(94\)90138-4](https://doi.org/10.1016/0022-1694(94)90138-4).
- French, M. M., H. B. Bluestein, I. PopStefanija, C. A. Baldi, and R. T. Bluth, 2014: Mobile, phased-array, Doppler radar observations of tornadoes at X band. *Mon. Wea. Rev.*, **142**, 1010–1036, <https://doi.org/10.1175/MWR-D-13-00101.1>.
- Gal-Chen, T., 1982: Errors in fixed and moving frame of references: Applications for conventional and Doppler radar analysis. *J. Atmos. Sci.*, **39**, 2279–2300, [https://doi.org/10.1175/1520-0469\(1982\)039<2279:EIFAMF>2.0.CO;2](https://doi.org/10.1175/1520-0469(1982)039<2279:EIFAMF>2.0.CO;2).
- Garabedian, P. R., 1998: *Partial Differential Equations*. 2nd ed. Chelsea Publishing Co., 672 pp.
- Germann, U., and I. Zawadzki, 2002: Scale-dependence of the predictability of precipitation from continental radar images. Part I: Description of the methodology. *Mon. Wea. Rev.*, **130**, 2859–2873, [https://doi.org/10.1175/1520-0493\(2002\)130<2859:SDOTPO>2.0.CO;2](https://doi.org/10.1175/1520-0493(2002)130<2859:SDOTPO>2.0.CO;2).
- Gerstner, E.-M., and G. Heinemann, 2008: Real-time areal precipitation determination from radar by means of statistical objective analysis. *J. Hydrol.*, **352**, 296–308, <https://doi.org/10.1016/j.jhydrol.2008.01.016>.
- Griffin, C. B., D. J. Bodine, J. M. Kurdzo, A. Mahre, and R. D. Palmer, 2019: High temporal resolution observations of the 27 May 2015 Canadian, Texas, tornado using the Atmospheric Imaging Radar. *Mon. Wea. Rev.*, **147**, 873–891, <https://doi.org/10.1175/MWR-D-18-0297.1>.
- Gustafson, K. E., 1987: *Introduction of Partial Differential Equations and Hilbert Space Methods*. 2nd ed. John Wiley and Sons, 409 pp.
- Harrison, D. L., R. W. Scovell, and M. Kitchen, 2009: High-resolution precipitation estimates for hydrological uses. *Proc. Inst. Civ. Eng. Water Manage.*, **162**, 125–135, <https://doi.org/10.1680/wama.2009.162.2.125>.
- Herrmann, R., 2011: *Fractional Calculus: An Introduction for Physicists*. World Scientific Publishing, 276 pp.
- Heymsfield, G. M., 1978: Kinematic and dynamic aspects of the Harrah tornadic storm analyzed from dual-Doppler radar data. *Mon. Wea. Rev.*, **106**, 233–254, [https://doi.org/10.1175/1520-0493\(1978\)106<0233:KADAOT>2.0.CO;2](https://doi.org/10.1175/1520-0493(1978)106<0233:KADAOT>2.0.CO;2).
- Higgins, C. W., M. Froidevaux, V. Simeonov, N. Vercauteren, C. Barry, and M. B. Parlange, 2012: The effect of scale on the applicability of Taylor's frozen turbulence hypothesis in the atmospheric boundary layer. *Bound.-Layer Meteorol.*, **143**, 379–391, <https://doi.org/10.1007/s10546-012-9701-1>.
- Hildebrand, P. H., and C. K. Mueller, 1985: Evaluation of meteorological airborne Doppler radar. Part I: Dual-Doppler analyses of air motions. *J. Atmos. Oceanic Technol.*, **2**, 362–380, [https://doi.org/10.1175/1520-0426\(1985\)002<0362:EOMADR>2.0.CO;2](https://doi.org/10.1175/1520-0426(1985)002<0362:EOMADR>2.0.CO;2).
- Isom, B., and Coauthors, 2013: The Atmospheric Imaging Radar: Simultaneous volumetric observations using a phased array weather radar. *J. Atmos. Oceanic Technol.*, **30**, 655–675, <https://doi.org/10.1175/JTECH-D-12-00063.1>.
- Kurdzo, J. M., B. L. Cheong, R. D. Palmer, G. Zhang, and J. B. Meier, 2014: A pulse compression waveform for improved-sensitivity weather radar observations. *J. Atmos. Oceanic Technol.*, **31**, 2713–2731, <https://doi.org/10.1175/JTECH-D-13-00021.1>.
- , and Coauthors, 2017: Observations of severe local storms and tornadoes with the Atmospheric Imaging Radar. *Bull. Amer. Meteor. Soc.*, **98**, 915–935, <https://doi.org/10.1175/BAMS-D-15-00266.1>.
- Lanczos, C., 1986: *The Variational Principles of Mechanics*. Dover, 418 pp.
- Laroche, S., and I. Zawadzki, 1995: Retrievals of horizontal winds from single-Doppler clear-air data by methods of cross correlation and variational analysis. *J. Atmos. Oceanic Technol.*, **12**, 721–738, [https://doi.org/10.1175/1520-0426\(1995\)012<0721:ROHWF>2.0.CO;2](https://doi.org/10.1175/1520-0426(1995)012<0721:ROHWF>2.0.CO;2).
- Lazarus, S., A. Shapiro, and K. Droegemeier, 2001: Application of the Zhang–Gal–Chen single-Doppler velocity retrieval to a deep convective storm. *J. Atmos. Sci.*, **58**, 998–1016, [https://doi.org/10.1175/1520-0469\(2001\)058<0998:AOTZGC>2.0.CO;2](https://doi.org/10.1175/1520-0469(2001)058<0998:AOTZGC>2.0.CO;2).
- Li, B., A. Murthi, K. P. Bowman, G. R. North, M. G. Genton, and M. Sherman, 2009: Statistical tests of Taylor's hypothesis: An application to precipitation fields. *J. Hydrometeorol.*, **10**, 254–265, <https://doi.org/10.1175/2008JHM1009.1>.
- Liou, Y.-C., 1999: Single radar recovery of cross-beam wind components using a modified moving frame of reference technique. *J. Atmos. Oceanic Technol.*, **16**, 1003–1016, [https://doi.org/10.1175/1520-0426\(1999\)016<1003:SRROCB>2.0.CO;2](https://doi.org/10.1175/1520-0426(1999)016<1003:SRROCB>2.0.CO;2).
- , 2007: Single Doppler retrieval of the three-dimensional wind in a deep convective system based on an optimal moving frame of reference. *J. Meteor. Soc. Japan*, **85**, 559–582, <https://doi.org/10.2151/jmsj.85.559>.
- , and I.-S. Luo, 2001: An investigation of the moving-frame single-Doppler wind retrieval technique using Taiwan Area Mesoscale Experiment low-level data. *J. Appl. Meteor.*, **40**, 1900–1917, [https://doi.org/10.1175/1520-0450\(2001\)040<1900:AIOTMF>2.0.CO;2](https://doi.org/10.1175/1520-0450(2001)040<1900:AIOTMF>2.0.CO;2).
- Liu, C., and W. F. Krajewski, 1996: A comparison of methods for calculation of radar-rainfall hourly accumulations. *J. Amer. Water Resour. Assoc.*, **32**, 305–315, <https://doi.org/10.1111/j.1752-1688.1996.tb03453.x>.

- Liu, S., C. Qiu, Q. Xu, and P. Zhang, 2004: An improved time interpolation for three-dimensional Doppler wind analysis. *J. Appl. Meteor.*, **43**, 1379–1391, <https://doi.org/10.1175/JAM2150.1>.
- Mahre, A., J. M. Kurdzo, D. J. Bodine, C. B. Griffin, R. D. Palmer, and T.-Y. Yu, 2018: Analysis of the 16 May 2015 Tipton, Oklahoma, EF-3 tornado at high spatiotemporal resolution using the Atmospheric Imaging Radar. *Mon. Wea. Rev.*, **146**, 2103–2124, <https://doi.org/10.1175/MWR-D-17-0256.1>.
- Matejka, T., 2002: Estimating the most steady frame of reference from Doppler radar data. *J. Atmos. Oceanic Technol.*, **19**, 1035–1048, [https://doi.org/10.1175/1520-0426\(2002\)019<1035:ETMSFO>2.0.CO;2](https://doi.org/10.1175/1520-0426(2002)019<1035:ETMSFO>2.0.CO;2).
- Mittermaier, M. P., R. J. Hogan, and A. J. Illingworth, 2004: Using mesoscale model winds for correcting wind-drift errors in radar estimates of surface rainfall. *Quart. J. Roy. Meteor. Soc.*, **130**, 2105–2123, <https://doi.org/10.1256/qj.03.156>.
- Nielsen, J. E., S. Thorndahl, and M. R. Rasmussen, 2014: A numerical method to generate high temporal resolution precipitation time series by combining weather radar measurements with a nowcast model. *Atmos. Res.*, **138**, 1–12, <https://doi.org/10.1016/j.atmosres.2013.10.015>.
- Oue, M., P. Kollias, A. Shapiro, A. Tatarevic, and T. Matsui, 2019: Investigation of observational error sources in multi-Doppler-radar three-dimensional variational vertical air motion retrievals. *Atmos. Meas. Tech.*, **12**, 1999–2018, <https://doi.org/10.5194/amt-12-1999-2019>.
- Oye, R., C. Mueller, and S. Smith, 1995: Software for radar translation, visualization, editing, and interpolation. Preprints, 27th Conf. on Radar Meteorology, Vail, CO, Amer. Meteor. Soc., 359–361.
- Press, W. H., S. A. Teukolsky, W. T. Vetterling, and B. P. Flannery, 1992: *Numerical Recipes in FORTRAN: The Art of Scientific Computing*. 2nd ed. Cambridge University Press, 963 pp.
- Qiu, C.-J., and Q. Xu, 1992: A simple adjoint method of wind analysis for single-Doppler data. *J. Atmos. Oceanic Technol.*, **9**, 588–598, [https://doi.org/10.1175/1520-0426\(1992\)009<0588:ASAMOW>2.0.CO;2](https://doi.org/10.1175/1520-0426(1992)009<0588:ASAMOW>2.0.CO;2).
- Rosenhead, L., Ed., 1963: *Laminar Boundary Layers*. Oxford University Press, 688 pp.
- Rudin, W., 1976: *Principles of Mathematical Analysis*. 3rd ed. McGraw-Hill, 342 pp.
- Sasaki, Y., 1970: Some basic formalisms in numerical variational analysis. *Mon. Wea. Rev.*, **98**, 875–883, [https://doi.org/10.1175/1520-0493\(1970\)098<0875:SBFINV>2.3.CO;2](https://doi.org/10.1175/1520-0493(1970)098<0875:SBFINV>2.3.CO;2).
- Seo, B.-C., and W. F. Krajewski, 2015: Correcting temporal sampling error in radar-rainfall: Effect of advection parameters and storm characteristics on the correction accuracy. *J. Hydrol.*, **531**, 272–283, <https://doi.org/10.1016/j.jhydrol.2015.04.018>.
- Shapiro, A., S. Ellis, and J. Shaw, 1995: Single-Doppler velocity retrievals with Phoenix II data: Clear air and microburst wind retrievals in the planetary boundary layer. *J. Atmos. Sci.*, **52**, 1265–1287, [https://doi.org/10.1175/1520-0469\(1995\)052<1265:SDVRWP>2.0.CO;2](https://doi.org/10.1175/1520-0469(1995)052<1265:SDVRWP>2.0.CO;2).
- , K. M. Willingham, and C. K. Potvin, 2010a: Spatially variable advection correction of radar data. Part I: Theoretical considerations. *J. Atmos. Sci.*, **67**, 3445–3456, <https://doi.org/10.1175/2010JAS3466.1>.
- , —, and —, 2010b: Spatially variable advection correction of radar data. Part II: Test results. *J. Atmos. Sci.*, **67**, 3457–3470, <https://doi.org/10.1175/2010JAS3466.1>.
- , S. Rahimi, C. K. Potvin, and L. Orf, 2015: On the use of advection correction in trajectory calculations. *J. Atmos. Sci.*, **72**, 4261–4280, <https://doi.org/10.1175/JAS-D-15-0095.1>.
- Siggia, A. D., and R. E. Passarelli, 2004: Gaussian model adaptive processing (GMAP) for improved ground clutter cancellation and moment calculation. *Proc. Third European Conf. on Radar Meteorology*, Visby, Sweden, ERAD, 67–73.
- Smull, B. F., and R. A. Houze, 1987: Dual-Doppler radar analysis of a midlatitude squall line with a trailing region of stratiform rain. *J. Atmos. Sci.*, **44**, 2128–2149, [https://doi.org/10.1175/1520-0469\(1987\)044<2128:DDRAOA>2.0.CO;2](https://doi.org/10.1175/1520-0469(1987)044<2128:DDRAOA>2.0.CO;2).
- Taylor, G. I., 1938: The spectrum of turbulence. *Proc. Roy. Soc. London*, **164A**, 476–490, <https://doi.org/10.1098/rspa.1938.0032>.
- Thorndahl, S., J. E. Nielsen, and M. R. Rasmussen, 2014: Bias adjustment and advection interpolation of long-term high resolution radar rainfall series. *J. Hydrol.*, **508**, 214–226, <https://doi.org/10.1016/j.jhydrol.2013.10.056>.
- Tuttle, J. D., and G. B. Foote, 1990: Determination of the boundary layer airflow from a single Doppler radar. *J. Atmos. Oceanic Technol.*, **7**, 218–232, [https://doi.org/10.1175/1520-0426\(1990\)007<0218:DOTBLA>2.0.CO;2](https://doi.org/10.1175/1520-0426(1990)007<0218:DOTBLA>2.0.CO;2).
- Uddin, A. K. M., A. E. Perry, and I. Marusic, 1997: On the validity of Taylor's hypothesis in wall turbulence. *J. Mech. Eng. Res. Dev.*, **19–20**, 57–66.
- Wienhoff, Z. B., H. B. Bluestein, L. J. Wicker, J. C. Snyder, A. Shapiro, C. K. Potvin, J. B. Houser, and D. W. Reif, 2018: Applications of a spatially variable advection correction technique for temporal correction of dual-Doppler analyses of tornadic supercells. *Mon. Wea. Rev.*, **146**, 2949–2971, <https://doi.org/10.1175/MWR-D-17-0360.1>.
- Wilczek, M., H. Xu, and Y. Narita, 2014: A note on Taylor's hypothesis under large-scale flow variation. *Nonlinear Processes Geophys.*, **21**, 645–649, <https://doi.org/10.5194/npg-21-645-2014>.
- Wurman, J., Y. Richardson, C. Alexander, S. Weygandt, and P. F. Zhang, 2007: Dual-Doppler analysis of winds and vorticity budget terms near a tornado. *Mon. Wea. Rev.*, **135**, 2392–2405, <https://doi.org/10.1175/MWR3404.1>.
- , K. A. Kosiba, P. Markowski, Y. Richardson, D. Dowell, and P. Robinson, 2010: Finescale single- and dual-Doppler analysis of tornado intensification, maintenance, and dissipation in the Orleans, Nebraska, supercell. *Mon. Wea. Rev.*, **138**, 4439–4455, <https://doi.org/10.1175/2010MWR3330.1>.
- Zawadzki, I. I., 1973: Statistical properties of precipitation patterns. *J. Appl. Meteor.*, **12**, 459–472, [https://doi.org/10.1175/1520-0450\(1973\)012<0459:SPOPP>2.0.CO;2](https://doi.org/10.1175/1520-0450(1973)012<0459:SPOPP>2.0.CO;2).
- Zhang, J., and T. Gal-Chen, 1996: Single-Doppler wind retrieval in the moving frame of reference. *J. Atmos. Sci.*, **53**, 2609–2623, [https://doi.org/10.1175/1520-0469\(1996\)053<2609:SDWRIT>2.0.CO;2](https://doi.org/10.1175/1520-0469(1996)053<2609:SDWRIT>2.0.CO;2).